Adsorption height determination of nonequivalent C and O species of PTCDA on Ag(110) using x-ray standing waves

G. Mercurio,[1,2,*] O. Bauer,[3] M. Willenbockel,[1,2] N. Fairley,[4] W. Reckien,[3] C. H. Schmitz,[3] B. Fiedler,[3] S. Soubatch,[1,2] T. Bredow,[3] M. Sokolowski,[3] and F. S. Tautz[1,2]

[1]*Peter Grünberg Institut (PGI-3), Forschungszentrum Jülich, 52425 Jülich, Germany*

[2]*Jülich Aachen Research Alliance (JARA), Fundamentals of Future Information Technology, 52425 Jülich, Germany*

[3]*Institut für Physikalische und Theoretische Chemie, Universität Bonn, 53115 Bonn, Germany*

[4]*Casa Software Ltd., Bay House, 5 Grosvenor Terrace, Teignmouth, Devon TQ14 8NE, United Kingdom*

(Received 1 October 2012; published 22 January 2013)

The normal incidence x-ray standing wave (NIXSW) technique is used to determine the adsorption geometry of submonolayer 3,4,9,10-perylene tetracarboxylic dianhydride (PTCDA) adsorbed on the Ag(110) surface. An accurate analysis of *both* C1*s* *and* O1*s* photoemission (PE) spectra allows the respective adsorption heights of carbon *and* oxygen atoms in different chemical environments within PTCDA to be distinguished. Due to the intricacy of the PE fitting models, a systematic error analysis of NIXSW structural parameters was developed and employed. Based on the adsorption geometry of PTCDA on Ag(110) a bonding mechanism is discussed.

DOI: 10.1103/PhysRevB.87.045421 PACS number(s): 68.43.Fg, 68.49.Uv, 82.80.Pv, 02.70.Uu

I. INTRODUCTION

In order to control the electronic properties of molecule/metal interfaces, a deep understanding of the adsorbate-substrate bonding mechanism is essential. This requires precise experimental data about both the geometric and the electronic interface structures. With regard to the geometric interface structure, the vertical molecular adsorption height above the substrate is an important parameter. The normal incidence x-ray standing wave (NIXSW) technique is the method of choice for determining adsorption heights on single-crystal surfaces.[1,2] Its advantages are that no lateral order is required, the fitting of experimental data for extracting structure parameters is model-free (unlike as in, e.g., LEED-*IV* analysis), a high precision of 0.05 Å in adsorption heights is routinely achievable, and the method has chemical sensitivity; that is, differential adsorption heights can be determined whenever two chemical species within the same molecule can be distinguished, for example, by their core level spectra.

The chemical sensitivity opens the window beyond pure molecular adsorption heights, because the internal distortion of the molecular adsorbate in response to adsorption becomes accessible. For molecules with various (functional) groups of distinct reactivity, this provides direct access to the chemistry of the interface, since, in principle, the NIXSW experiment can reveal which parts of the molecule approach the substrate most closely. Clearly, this provides valuable information for the development of bonding models. However, it is not straightforward to take advantage of this principal capability of NIXSW for organic molecules, because the same small set of atomic species (typically carbon, oxygen, nitrogen, etc.) appears in all parts of the molecule, and to fully exploit the potential of the NIXSW method, signals of the same element in different chemical environments must be separated.

This is the challenge which we address in the current paper, using the commonly employed model molecule 3,4,9,10-perylene tetracarboxylic dianhydride (PTCDA) as an example. In the field of organic electronics, PTCDA has been widely studied as a prototype of a functionalized π-conjugated molecule, because it consists of a perylene core and two functional groups.[3] On Au(111) (Ref. 4), Ag(111) (Refs. 5–7), and Cu(111) (Ref. 8) PTCDA adsorption has already been studied with NIXSW.

In the pioneering work of Sugiyama *et al.*[9] XSW was used for the first time to locate atoms of the same element in different compounds, hence in different chemical environments. The basic idea was to exploit the corresponding chemical shifts and extract the structural information from the respective photoemission (PE) peaks. The same principle was employed for a number of other systems, always with the aim to differentiate the positions of the same atomic element in various coadsorbed molecular species.[10–13] Similar structural and chemical-state specific information is also obtainable by using photoelectron diffraction.[14,15]

In the case of PTCDA adsorption, NIXSW was already used to discriminate atoms in different chemical state within the same molecule [PTCDA on Ag(111) (Refs. 5–7) and on Cu(111) (Ref. 8)]. However, so far only the differentiation between two types of oxygen atoms (carboxylic and anhydride oxygens) of PTCDA was possible. The chemical shift between the two is 2.5 eV, and the two O1*s* peaks are clearly separable in the XPS spectra by eye. Here we study PTCDA on Ag(110) and extend the data analysis from differential oxygen heights to differential carbon heights; namely we separate the carboxylic or functional carbon from the rest of the perylene skeleton. Although the relevant C1*s* chemical shift is still approximately 2.1 eV, this task is much more challenging, since peaks are not separable by eye and the intensity ratio of 1:5 is much less amenable than in the case of the oxygens (1:2), as we show below. Therefore, it requires the development of an elaborate fitting model (including careful background subtraction and the consideration of line shape and satellites) and an involved error analysis to safeguard the meaningfulness of the results.

On the open and anisotropic Ag(110) surface, PTCDA forms a brick-wall structure that is commensurate with the substrate, as is known from low-energy electron diffraction (LEED) and scanning tunneling microscopy (STM) experiments.[16,17] The commensurability together with a well-defined unique adsorption site, deduced from STM,[17] suggests

a chemical bond between PTCDA and the surface Ag atoms. A further indication to this effect comes from ultraviolet photoemission spectroscopy (UPS), which reveals a charge transfer from the substrate to the molecule upon adsorption.[18] Its relatively strong reactivity makes Ag(110) well suited for the present purpose of differentially fitting oxygen *and* carbon species, since presumably clear distortions of the molecule result from the strong interaction with the surface. However, differential fitting using the same procedure as introduced here has also been demonstrated for PTCDA on the less reactive Ag(100) surface.[19,20]

As a result of our NIXSW experiments and the analysis detailed in this paper, we find that on Ag(110) PTCDA distorts strongly. The complete functional groups, including all oxygen atoms and the carbon atoms bonded to the oxygens, bend towards the surface. This is similar to the known case of PTCDA/Ag(111),[5–7] where the carboxylic oxygens move towards the surface. However, there are characteristic differences between Ag(111) and Ag(110), both in the average PTCDA bonding height, which is substantially smaller on Ag(110) than on Ag(111), and with respect to the resulting shape of the molecule on the surface. In the case of Ag(111), PTCDA adsorbs in a saddlelike configuration, with the anhydride oxygens above the average height of the carbon backbone, while on Ag(110) PTCDA adopts an archlike shape, with all oxygen below the carbons of the functional groups and below the average height of the perylene core. These characteristic differences in adsorption heights and adsorption shapes can be used to derive a detailed bonding model for PTCDA on silver surfaces. This is discussed in Ref. 20. In the present paper, in contrast and complementary to Ref. 20, we focus on the elaborate data analysis which is required to extract the structures from the experiments and briefly discuss the findings.

The paper is organized as follows. Section II provides the experimental details including the preparation of the sample, the acquisition and analysis of x-ray photoemission spectroscopy (XPS) and NIXSW data. A detailed description of how errors are calculated and interpreted is given in Sec. II B4. The experimental results, that is, PE spectra, PE yields, and corresponding structural parameters, that is, coherent position and coherent fraction (P_c, F_c), of silver, carbon, and oxygen are presented in Sec. III. Section IV reports the discussion of the adsorption geometry of PTCDA on Ag(110) and the interpretation of its coherent fraction. Finally, experimental results are compared to *ab initio* calculations and a bonding model is discussed (Sec. IV C).

II. EXPERIMENTAL DETAILS

A. Sample preparation

NIXSW experiments were performed at the beamline ID32 of the European Synchrotron Radiation Facility (ESRF, Grenoble). A sketch of the experimental setup can be found in Fig. 1. Since we are interested in the direct interaction of PTCDA with the Ag(110) surface, we intend to study the bonding geometry of PTCDA in the submonolayer regime, that is, when the sample coverage is less than one monolayer (ML).[21] This ensures that NIXSW results are not influenced by the second layer.

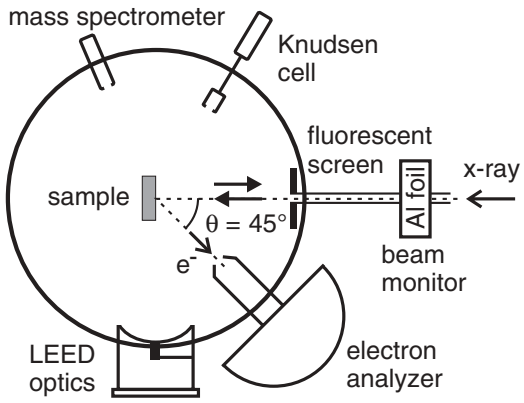

FIG. 1. Schematic top-view section of the UHV chamber at the beamline ID32 (ESRF) in which NIXSW experiments were performed.

A submonolayer of PTCDA/Ag(110) was prepared in the following way. The Ag(110) crystal was cleaned by repeated cycles of Ar^+ sputtering and annealing at 600 °C. The cleanliness of the crystal was checked by LEED and XPS. Successively, PTCDA molecules were evaporated from a Knudsen cell onto the Ag substrate kept at room temperature. Finally, the sample was annealed at 420 K for several minutes in order to increase the homogeneity of the molecular layer. NIXSW experiments were performed on the PTCDA/Ag(110) sample at room temperature.

The only way to obtain a submonolayer PTCDA/Ag(110) phase of a pure brick-wall structure is to directly deposit <1 ML on the surface. Desorption of PTCDA multilayers from Ag(110) yields a compact layer of two coexisting phases, namely brick wall [Fig. 2(b)] and herringbone, as LEED and STM experiments show.[22,23] Moreover, PTCDA molecules in the first layer cannot be desorbed before dissociation at more than 550 K.[18,24] To prove that the sample consists only of <1 ML brick-wall PTCDA phase, we calculate the molecular coverage θ and additionally monitor the corresponding structure with LEED.

To estimate the coverage of the sample, the ratio of the photoelectron yields Y_{Zj} and $Y_{Z'j'}$ (i.e., of integrated PE intensities after background subtraction) of two lines j and j' with kinetic energies E_k and E'_k emitted by the two elements

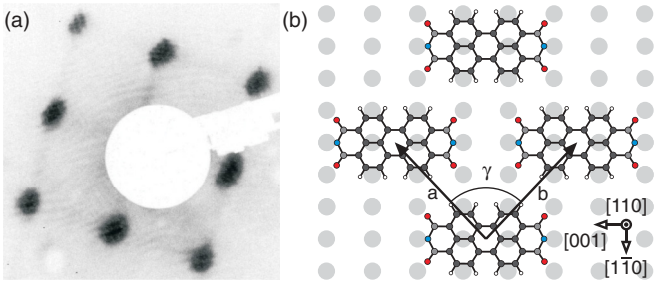

FIG. 2. (Color) (a) LEED image (with electron beam energy of 19 eV) of the PTCDA/Ag(110) brick-wall phase on which NIXSW experiments were performed. The corresponding superstructure matrix is (2 3 | −2 3). (b) Schematic view of the brick-wall unit cell, with $a = b = 11.9$ Å and $\gamma = 86.7°$ (Ref. 17).

Z and Z' is considered[25]:

$$\frac{Y_{Zj}}{Y_{Z'j'}} = \frac{\sigma_{Zj} C_Z \lambda(E_k) T(E_k) \exp[-\langle d\rangle/\lambda(E_k)]}{\sigma_{Z'j'} C_{Z'} \lambda(E'_k) T(E'_k) \exp[-\langle d'\rangle/\lambda'(E'_k)]}. \quad (1)$$

Here, σ_{Zj} and $\sigma_{Z'j'}$ are the respective photoionization cross sections and C_Z and $C_{Z'}$ the atomic concentrations. $\lambda(E_k)$ is the mean electron escape depth for electrons with kinetic energy E_k. $T(E_k)$ is the analyzer transmission at kinetic energy E_k. Finally, the exponential factor describes the attenuation of the photoelectron intensity through surface layers of effective thicknesses $\langle d\rangle$ and $\langle d'\rangle$ for photoelectrons from the two different elements.

The thickness of the PTCDA layer is estimated by comparing the PE yield of C1s and Ag3d lines, that is, Y_{C1s} and Y_{Ag3d}. Since the kinetic energy E_k of C1s photoelectrons is only 2% larger than that of Ag3d photoelectrons, electron escape depths and analyzer transmissions are approximately equal for these two lines; therefore, the corresponding factors λ and T cancel out. Moreover, the thickness of the layer crossed by substrate photoelectrons is $\langle d'\rangle \approx \langle d\rangle \approx 0$, where $\langle d\rangle$ is approximated with zero because we did not deposit much more than 1 ML. As a consequence, both exponential terms are approximately 1. Within the approximations discussed above, Eq. (1) reduces to the following relation between the concentrations of carbon ($C^{C}_{Ag(110)}$) and silver ($C^{Ag}_{Ag(110)}$), estimated through C1s and Ag3d lines:

$$\frac{C^{C}_{Ag(110)}}{C^{Ag}_{Ag(110)}} \propto \frac{Y_{C1s}}{Y_{Ag3d}} \frac{\sigma_{Ag3d}}{\sigma_{C1s}}. \quad (2)$$

We consider the sample obtained by thermal desorption of a PTCDA multilayer from the Ag(111) surface as a reference for a 1-ML PTCDA film.[6] The latter desorption experiment was performed with the same experimental setup (Fig. 1) during a previous beam time. The corresponding 1-ML $C^{C}_{Ag(111)}/C^{Ag}_{Ag(111)}$ ratio is corrected for the different molecular densities of the PTCDA herringbone phase on Ag(111) ($\rho_{herringbone} = 8.35 \times 10^{13}$ molecules cm^{-2}) and of the PTCDA brick-wall phase on Ag(110) ($\rho_{brickwall} = 7.06 \times 10^{13}$ molecules cm^{-2}).[17] The resulting sample coverage of PTCDA on Ag(110) on which NIXSW experiments were performed, that is,

$$\theta = \frac{C^{C}_{Ag(110)}/C^{Ag}_{Ag(110)}}{C^{C}_{Ag(111)}/C^{Ag}_{Ag(111)}} \frac{\rho_{herringbone}}{\rho_{brickwall}}, \quad (3)$$

is 0.89 ± 0.09. The corresponding LEED image and unit cell, characteristic of the brick-wall phase, are shown in Fig. 2.

B. NIXSW data acquisition and analysis

1. PE spectra and PE yield

An NIXSW data set consists of x-ray photoemission spectra measured at different photon energies ($h\nu$) around the Bragg condition ($h\nu = E_{Bragg}$) (XSW-PE spectra) and the corresponding x-ray reflectivity curve. Each XSW-PE spectrum is normalized to the intensity of the incoming beam that is measured through the photoelectron current generated on an Al foil located in the beam path (Fig. 1). For each $h\nu$ the intensity of the x-ray beam reflected from the sample crystal is measured through the photoelectron current generated on a fluorescent screen located at a small angle close to the incoming beam (Fig. 1).

For the fcc Ag crystal the structure factor corresponding to the (110) reflection vanishes; hence, the intensity of that reflection is zero.[26] Therefore, we utilized in our experiments the reflection from the (220)-Bragg planes, corresponding to a Bragg energy of 4294.6 eV, at which both C1s and O1s photoionization cross sections are rather low.[27] Because of this and to prevent beam damage, XSW-PE spectra could not be recorded with high resolution. Nevertheless, in order to analyze nonequivalent carbon and oxygen species separately, high-statistics PE spectra (HS-PE spectra) with smaller kinetic energy step (0.1 eV) and larger counting time (500 ms) than for the XSW-PE spectra (0.2 eV and 100 ms) were recorded to develop the fitting model for XSW-PE spectra. HS-PE spectra were acquired at off-Bragg condition with $h\nu = 4280$ eV in order to avoid the standing wave effect. The pass energies of HS-PE and XSW-PE spectra were 47 eV. The number of repeats of C1s (O1s) HS-PE and XSW-PE spectra was equal to 4 (13) and 6 (7), respectively. The energy window of C1s (O1s) HS-PE and XSW-PE spectra was equal to 40 eV (20 eV) and 31 eV (26 eV), respectively. As a general approach, followed for both C1s and O1s spectra (Secs. III B and III C), fitting models were derived on HS-PE spectra and then transferred to XSW-PE spectra.

For a higher reliability of the C1s fitting model, by which a small chemical shift of nonequivalent C atoms needs to be resolved, C1s spectra were additionally measured with higher resolution (HR-PE spectra). In particular, we used an XPS setup including a monochromated Al $K\alpha$ laboratory source (1486 eV) and a Scienta R4000 analyzer, and providing the full width at half maximum (FWHM) of the Ag3$d_{5/2}$ line of $\Delta E = 0.65$ eV. Because of the smaller photon energy of the laboratory source, the C1s photoionization cross section (13.67 kb) is approximately 25 times larger than the one corresponding to the photon energy in our NIXSW experiments (0.53 kb).[27] This leads to spectra with better signal-to-noise ratio and facilitates the differentiation of chemically shifted C1s peaks, as discussed in Sec. III B. C1s HR-PE spectra were recorded with a pass energy of 200 eV, an energy window of 20 eV, an energy step of 0.1 eV, a time/step = 500 ms, and 10 repeats.

To confirm the validity of the C1s fitting model developed by Schöll *et al.*[28] on the basis of PE spectra of a PTCDA multilayer film (>10 ML) adsorbed on Ag(111) (HR-mL-PE spectrum), measured at the U49/1-PGM beamline at BESSY II with $h\nu = 335$ eV, we acquired a PE spectrum of approximately 40 ML PTCDA adsorbed on Ag(100) (mL-PE spectrum) with the experimental setup shown in Fig. 1. The mL-PE spectrum was recorded at $h\nu = 3024$ eV, 11 eV below the Bragg energy of the (200) reflection. The corresponding acquisition settings were as follows: pass energy = 11.75 eV, energy window = 25 eV, energy step = 0.1 eV, time/step = 100 ms and 25 repeats. Because of the larger C1s photoionization cross section (due to the smaller photon energy) and the thus better signal-to-noise ratio, we have considered here a PTCDA multilayer spectrum recorded on the Ag(100) surface rather than on the Ag(110) surface. However, we expect the C1s spectrum of a thick PTCDA multilayer to be independent of the orientation of the Ag surface. This is confirmed by

the good agreement of the C1*s* fitting model developed for multilayer PTCDA on Ag(111)[28] with the C1*s* PE spectrum of multilayer PTCDA on Ag(100) [cf. Fig. 6(b)].

All PE spectra are analyzed with the software CASAXPS[29] that provides as output the component areas $Y_{Zj\gamma}$ [of element Z, PE line (core level) j, component γ] after background subtraction and the corresponding errors. The component areas $Y_{Zj\gamma}$ are obtained by means of the Levenberg-Marquardt algorithm that minimizes the residuals between the synthetic data envelope, that is, the sum of the fitting components $I_{Zj\gamma}(E_i)$ for a given element Z and PE line j and the experimental data.

The PE yield $Y_{Zj\gamma}$ for each component as a function of the incoming photon energy $h\nu$ carries the structural information about the corresponding photoemitter, that is, its coherent position P_c and its coherent fraction F_c. P_c corresponds to the average adsorption height of the photoemitter $Zj\gamma$ with respect to the nearest (extended) Bragg plane underneath, while F_c is related to the amplitude of the corresponding height distribution.[30] Both structural parameters may acquire values between 0 and 1. The larger the distribution of photoemitters normal to the Bragg planes, the smaller is F_c. P_c is defined modulo 1; thus, $P_c = 0$ and $P_c = 1$ are equivalent and correspond to a (extended) Bragg plane position, while $0 < P_c < 1$ refers to a vertical site between two consecutive (extended) Bragg planes. The fitting of the PE yield profiles $Y_{Zj\gamma}(h\nu)$ in Sec. III is performed by means of the XSW analysis software TORRICELLI,[31,32] the details of which will be published elsewhere.[33] Results identical (within the errors) to the ones reported in Sec. III are obtained by the program XSWAVES.[34]

2. Background determination

The relevant quantity in XSW data analysis is the PE yield $Y_{Zj\gamma}(h\nu)$, defined as the difference between the PE intensity of a certain adsorbate line $Zj\gamma$ in a set of XSW-PE spectra and the background. For thin adsorbate layers, the background originates almost exclusively from the substrate. For an accurate calculation of an adsorbate PE yield, it is essential to properly define the background in the corresponding energy range, in order to prevent a portion of the substrate signal from being included in the adsorbate PE yield and thus the adsorbate structural parameters from being altered by the contribution from the substrate.

For all PE spectra discussed in Sec. III a linear background,

$$B(E_i) = I_n \frac{E_{n+r} - E_i}{E_{n+r} - E_n} + I_{n+r} \frac{E_i - E_n}{E_{n+r} - E_n}, \tag{4}$$

is used. Here, E_i, with $i = 1, \ldots, n, \ldots, n+r, \ldots, N$, are the positions on the kinetic energy (or binding energy) axis at which the photoelectron intensity has been measured, and $I_n \equiv I^{\exp}(E_n)$ and $I_{n+r} \equiv I^{\exp}(E_{n+r})$ are the PE intensities corresponding to the energies E_n and E_{n+r}, which, in turn, refer to the boundaries of the selected energy window over which the spectrum is going to be fitted (Fig. 3). In order to prevent the statistical noise from affecting the background definition, the intensities I_n and I_{n+r} are replaced by the averages $\langle I_n \rangle$ and $\langle I_{n+r} \rangle$ over the experimental spectrum $I^{\exp}(E_i)$ that include $2m + 1$ points around E_n and E_{n+r},[35]

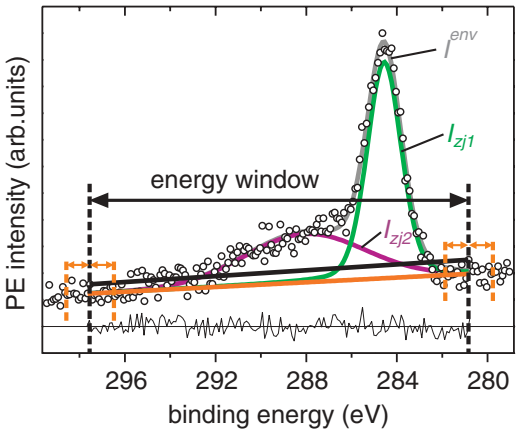

FIG. 3. (Color) C1*s* PE spectrum $I^{\exp}$ (open circles) of submonolayer PTCDA/Ag(110) with two fitting components I_{Zj1} (green line) and I_{Zj2} (magenta line) and the envelope $I^{\text{env}} = I_{Zj1} + I_{Zj2}$ (gray line). The black line below the spectrum indicates the residuals ($I^{\exp} - I^{\text{env}}$). The orange (black) straight line marks the linear background with $m = 10$ ($m = 0$) (see text).

that is,

$$\langle I_q \rangle = \frac{1}{2m+1} \sum_{i=q-m}^{q+m} I^{\exp}(E_i), \tag{5}$$

with $q = n, n+r$. m is a tunable parameter defining the number of data points to the left and to the right of the data points $I^{\exp}(E_q)$ that are included in the average. The optimum m results from a compromise between two contrasting requirements. On the one hand, the desire to improve the robustness of the background against the statistical noise requires larger m. On the other hand, m must be small enough to prevent $\langle I_q \rangle$ from containing adsorbate signal, since our goal is to decouple adsorbate from substrate contributions. Figure 3 shows an example of an erroneous background definition corresponding to $m = 0$ (black line) and a more accurate linear background obtained with $m = 10$ (orange line).

3. Line shape of the fitting components

The line shape of a core-level PE peak in XSW-PE or HS-PE spectra is the result of a combination of the physics involved in the photoelectric effect and the measurement process. The latter includes, for example, the response function of the electron analyzer, the profile of the x-ray beam, and thermal broadening and is modeled by Gauss functions. In contrast, Lorentzians are used to account for the lifetime broadening due to the uncertainty principle that relates the lifetime of the core hole to the energy uncertainty of the photoemitted electrons. We employ Voigt profiles approximated by the linear combination of a Gauss and a Lorentz function to model each individual fitting component,

$$\begin{aligned} &I_{Zj\gamma}(E_i; E_{Zj\gamma}, W_{Zj\gamma}, Y_{Zj\gamma}) \\ &\quad = (1-p) \frac{Y_{Zj\gamma}}{W_{Zj\gamma}} \exp\left[-4 \ln 2 \frac{(E_i - E_{Zj\gamma})^2}{W_{Zj\gamma}^2} \right] \\ &\qquad + p \frac{Y_{Zj\gamma}/W_{Zj\gamma}}{1 + 4\frac{(E_i - E_{Zj\gamma})^2}{W_{Zj\gamma}^2}}, \end{aligned} \tag{6}$$

that is used to describe an experimental PE spectrum $I_{Zj}(E_i)$.[36] Here, $E_{Zj\gamma}$ and $W_{Zj\gamma}$ are the energy position and the FWHM of the component $I_{Zj\gamma}$, while $Y_{Zj\gamma}$ is its peak area. The mixing parameter p allows the line shapes of $I_{Zj\gamma}$ to be tuned to better describe the measured PE line $I_{Zj}(E_i)$.

The fitting components of the PE spectra reported in Sec. III are categorized as main (m) peaks, that is, the most intense features, and satellite (s) peaks. The latter appear at higher binding energies than the corresponding main peaks and are assigned to shakeup processes in which the primary photoelectrons lose part of their kinetic energy to excitations of valence electrons into unoccupied molecular orbitals.[28] We find that the best fit of our PE spectra is obtained with Voigt functions ($p = 0.2$) for the main peaks and pure Gaussians ($p = 0$) for the satellite peaks. Attempts to use Voigt functions also for the satellite peaks yield identical structural parameters P_c and F_c (within the errors). Therefore, we conclude that for the purpose of the PE yield calculation, the specific line shape of the fitting component does not play a crucial role.

4. Error analysis

Little attention is usually given to the statistical precision of the structural parameters P_c and F_c. Error bars of the order of 0.05 Å are often quoted for the adsorption heights derived from the coherent positions P_c.[37,38] Because of the intricate fitting models employed in the present work (cf. Secs. III B and III C), we consider the statistical significance of our multicomponent fits of XSW-PE spectra carefully and propagate their uncertainty into the statistical error of the structural parameters P_c and F_c.

A quantitative analysis of XSW-PE spectra involves both statistical and systematic errors. There are several possible causes of systematic errors in the determination of P_c and F_c. These are, for example, (1) an incorrect decomposition of the XSW-PE spectrum into multiple components, (2) inaccurate nondipolar parameters which enter directly the fitting function $Y^{\text{theo}}_{Zj\gamma}(h\nu)$ of the PE yield profile,[37,41] or (3) a drifting incident x-ray beam that becomes misaligned with respect to the analyzer and hence leads to a wrong normalization of the PE yield by an x-ray intensity that is too large. Since measurements of the nondipolar parameters may lead to ambiguous results,[8,38,42] in Sec. III only calculated values (Table I) are employed. In fact, nondipolar parameters can be calculated for photoelectrons from s shells.[39] In particular, S_R can be calculated via a generalized formula that is valid for all l shells,[37,41] while $|S_I|$ and Ψ are dependent on the parameter Δ, which is not known for $l \neq 0$. Therefore, nondipolar parameters are not taken into account here for Ag3d core levels ($S_R = 1, |S_I| = 1, \Psi = 0$).[43]

TABLE I. Nondipolar parameters Q, Δ and S_R, $|S_I|$, Ψ calculated for C1s and O1s lines according to formulas in Refs. 37 and 39 γ is the angular distribution parameter (Ref. 27). δ_p and δ_d are the scattering phase shifts for p- and d- asymptotic waves, available from *ab initio* calculations (Ref. 40).

	γ	δ_p	δ_d	Q	Δ	S_R	$\lvert S_I\rvert$	Ψ
C1s	1.421	0.6928	0.5267	0.335	−0.166	2.007	1.506	−0.056
O1s	1.351	0.8720	0.6445	0.319	−0.228	1.935	1.471	−0.074

Statistical errors originate from the statistical noise that affects the photoelectron detection. This noise follows the Poisson counting statistics.[44] Although systematic errors may well be larger than statistical errors, in comparative studies of two or more spectra that are acquired under the same experimental conditions, statistical errors become important and ultimately define the significance of the XSW-PE spectrum fitting parameters. We focus below on the statistical error. In particular, in Sec. II B4a we derive the statistical error of the PE yield which is then propagated to calculate the error of P_c and F_c, as described in Sec. II B4b.

(a) Statistical error of the PE yield. Let us consider a PE spectrum $I^{\text{exp}}(E_i)$ consisting of N data points which can be decomposed into multiple overlapping components $I_\gamma(E_i;\mathbf{a}_\gamma)$, where $\mathbf{a}_\gamma$ represents the fitting parameters of the component γ, that is, $\mathbf{a}_\gamma = (E_\gamma, W_\gamma, Y_\gamma)$ (Sec. II B3), with Y_γ being the PE yield of $I_\gamma(E_i;\mathbf{a}_\gamma)$. The envelope $I^{\text{env}}(E_i)$ of Γ fitting components is given by

$$I^{\text{env}}(E_i;\mathbf{a}) = \sum_{\gamma=1}^{\Gamma} I_\gamma(E_i;\mathbf{a}_\gamma), \tag{7}$$

where $\mathbf{a} = (\mathbf{a}_1, \ldots, \mathbf{a}_\Gamma)$ represents all fitting parameters whose maximal number is $M = 3\Gamma$, if for each component γ all three parameters $(E_\gamma, W_\gamma, Y_\gamma)$ are left free to be fitted. The best fit of $I^{\text{exp}}(E_i)$ corresponds to the minimum of the quantity

$$\chi^2 \equiv \sum_{i=1}^{N} \left(\frac{I^{\text{exp}}(E_i) - I^{\text{env}}(E_i;\mathbf{a})}{\sigma_i} \right)^2, \tag{8}$$

with $\sigma_i = \sqrt{I^{\text{exp}}(E_i)}$ (Ref. 35)

Due to the nonlinear dependence of the fitting function $I^{\text{env}}(E_i;\mathbf{a})$ on the fitting parameters $\mathbf{a}$ [Eq. (6)], the χ^2 minimization must proceed iteratively starting from an initial guess for $\mathbf{a}$. For this purpose we use the Levenberg-Marquardt algorithm which calculates the Hessian matrix as a by-product.[45] The inverse of the Hessian matrix is the $M \times M$ covariance matrix $\mathbf{C}$. The square roots of the covariance matrix's diagonal elements represent the standard deviations of the fitting parameters $\sigma(a_\mu) = \sqrt{\mathbf{C}_{\mu\mu}}$, where $\mu = 1, \ldots, M$ and a_μ indicates any of the M fitting parameters in the parameter set $\mathbf{a}$. However, $\sigma(a_\mu)$ can be considered a good estimate of the error of a_μ only if fitting parameters are uncorrelated. This is certainly not true for overlapping components $I(E_i;\mathbf{a}_\gamma)$ in PE spectra (see, e.g., the spectrum in Fig. 3). Moreover, the Hessian matrix is often singular; thus, its inverse cannot be computed.[45]

For these reasons we employ a different approach to determine the errors $\sigma(a_\mu)$. The latter could be easily calculated if a large number of independently measured spectra $I^{\text{exp}}(E_i)$ was available, each of which could be fitted with the same fitting model. For each parameter a_μ, an average $\langle a_\mu \rangle$ and a standard deviation $\sigma(a_\mu)$ could then be computed. However, this approach cannot be implemented due to the small number of the available experimental spectra $I^{\text{exp}}(E_i)$. To overcome this problem, we generate, starting from the experimental $I^{\text{exp}}(E_i)$, a large number of synthetic spectra $I^{\text{MC}}(E_i)$ by a

Monte Carlo algorithm, assuming that the noise of the PE intensity follows a Poisson distribution.

The assumption of Poisson statistics for our PE intensity was verified as follows. In counting experiments, according to Poisson statistics, the mean is the number of counts $I^{\exp}(E_i)$ and the standard deviation is $\sqrt{I^{\exp}(E_i)}$ (Ref. 46). For large $I^{\exp}(E_i)$, a Poisson distribution is well approximated by a Gaussian distribution, with mean and standard deviation equal to $I^{\exp}(E_i)$ and $\sqrt{I^{\exp}(E_i)}$, respectively.[47] We considered then, as an example and for simplicity, a flat region of a PE spectrum that can be fitted with a horizontal line, for example, the energy window 279–282 eV in Fig. 3. After fitting the spectrum with a horizontal line, we computed the residual, that is, subtracted the actual data from the fitted line. Next, we calculated the standard deviation of the residual from the fitted line. If the experimental data follow Poisson statistics, the standard deviation of the residual, divided by $\sqrt{I^{\exp}(E_i)}$, should give 1. This was fulfilled.

We employ the software CASAXPS[29] to perform the Monte Carlo-based error analysis. In detail, the analysis proceeds as follows[45]: (i) The spectrum $I^{\exp}(E_i)$ is fitted by χ^2 minimization, and the resulting envelope $I^{\text{env}}(E_i;\mathbf{a})$ represents the basis for the generation of the synthetic spectra. (ii) A uniform pseudorandom sequence of synthetic values is generated for each $i = 1,\ldots,N$. From this, a synthetic PE spectrum $I^{\text{MC}_1}(E_i)$ with pseudorandom noise is generated, which fulfills for each i a Gaussian distribution with mean and standard deviation equal to $I^{\text{env}}(E_i;\mathbf{a})$ and $\sqrt{I^{\text{env}}(E_i;\mathbf{a})}$, respectively.[45] (iii) $I^{\text{MC}_1}(E_i)$ is fitted using the fitting function $I^{\text{env}}(E_i;\mathbf{a})$ by minimizing the quantity

$$\chi^2 \equiv \sum_{i=1}^{N}\left(\frac{I^{\text{MC}_1}(E_i) - I^{\text{env}}(E_i;\mathbf{a})}{\sigma_i}\right)^2, \tag{9}$$

where $\sigma_i = \sqrt{I^{\text{MC}_1}(E_i)}$. The resulting fitting parameters $\mathbf{a}^{\text{MC}_1}$ differ from the original set $\mathbf{a}$ from step (i) only because a different random noise is present in $I^{\text{MC}_1}(E_i)$ as compared to $I^{\exp}(E_i)$. Hence, this new parameter set $\mathbf{a}^{\text{MC}_1}$ is fully consistent with the measured spectrum $I^{\exp}(E_i)$. (iv) In order to have good statistics, 400 synthetic spectra $I^{\text{MC}_\tau}(E_i)$ are generated and as many fitted parameter sets $\mathbf{a}^{\text{MC}_\tau}$ are determined following steps (ii) and (iii).

From the distribution of parameter sets $\mathbf{a}^{\text{MC}_\tau}$ for $\tau = 1,\ldots,400$ the error of each fitting parameter a_μ can be determined. This proceeds as follows. In the M-dimensional space of the fitting parameters a_μ we select as a region of confidence the ellipsoid that contains 68.3% of the total $\mathbf{a}^{\text{MC}_\tau}$ distribution. The confidence level of 68.3% is the probability of finding a value within $\pm$ the standard deviation of the mean value for a normal distribution. In the coordinate system $(t_1,\ldots,t_M)$ of its principal axes the ellipsoid is given by[48]

$$\frac{t_1^2}{\rho_1^2} + \cdots + \frac{t_M^2}{\rho_M^2} = 1, \tag{10}$$

where the ρ_μ is the μth semiaxes of the ellipsoid. Projecting the error ellipsoid onto the axis a_μ, one obtains the confidence interval $2\sigma_\mu$ of the fitting parameter a_μ. Note that errors calculated in this manner account also for the correlations among the fitting parameters because the ellipsoid represents all fitting parameters simultaneously. Moreover, the Monte Carlo method allows the influence of the noise on the background and in turn on all other fitting parameters to be taken into account by the corresponding σ_μ.

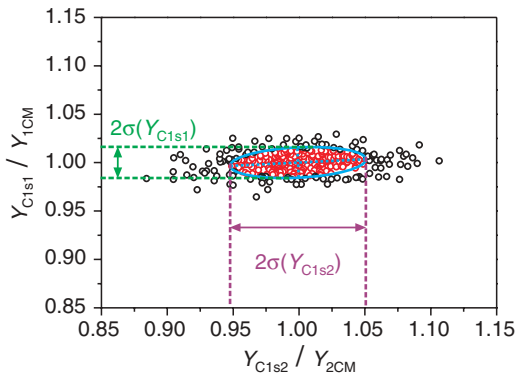

FIG. 4. (Color) Plot of the $(Y_{C1s1}, Y_{C1s2})^{MC}$ distribution resulting from the fit of 400 Monte Carlo simulations of the spectrum in Fig. 3. The blue ellipse contains all points of the distribution that lie within the confidence region (68.3% of all points). The center of the ellipse is the center of mass (CM) of the distribution. The principal axes are indicated by dotted blue lines. Points within the confidence region are represented by red open circles; those outside are marked by black open circles. The confidence interval of the two fitting parameters $2\sigma(Y_{C1s1})$ and $2\sigma(Y_{C1s2})$ are marked by dashed lines. Note that the axes are normalized to the PE yields of the center of mass (Y_{1CM}, Y_{2CM}).

As an example, we refer to the C1s spectrum $I^{\exp}(E_i)$ in Fig. 3 that has been fitted by two components ($\gamma = 1,2$). The envelope is given by $I^{\text{env}}(E_i; Y_{C1s1}, Y_{C1s2}) = I_1(E_i; Y_{C1s1}) + I_2(E_i; Y_{C1s2})$. The remaining possible fitting parameters E_{C1s1}, E_{C1s2}, W_{C1s1}, W_{C1s2} are not included, because they are fixed. Monte Carlo simulations of $I^{\exp}$ are performed and the resulting $(Y_{C1s1}, Y_{C1s2})^{MC}$ distribution is shown in Fig. 4. The ellipse representing the two-dimensional confidence region is marked in blue and all the parameter sets within it are marked in red. The confidence intervals of Y_{C1s1} and Y_{C1s2} are approximately $\pm 2\%$ and $\pm 5\%$ of the best fit values resulting from the minimization of χ^2 as in Eq. (8) with $\mathbf{a}^{\exp} = (Y_{C1s1}^{\exp}, Y_{C1s2}^{\exp})$.

(b) Statistical error of P_c and F_c. The result of the fitting of XSW-PE spectra and of the corresponding Monte Carlo-based error analysis are experimental yield curves $Y^{\exp}(h\nu_l)$ as a function of photon energy $h\nu_l$ ($l = 0,\ldots,P$) for all relevant components γ of element Z, PE line j (indices not shown), including an error bar σ_l at each photon energy. σ_l is the corresponding error of the PE yield at photon energy $h\nu_l$ that is calculated by the Monte Carlo-based analysis as detailed above. In the next step, these yield curves are fitted with a function $Y^{\text{theo}}(h\nu_l; P_c, F_c, N_0)$. $Y^{\text{theo}}(h\nu_l; P_c, F_c, N_0)$ is the theoretical expression for the photon-energy-dependent PE yield in NIXSW,[37,39] with the two structural parameters P_c and F_c and an overall normalization factor N_0 as fitting parameters. The exact expression of $Y^{\text{theo}}(h\nu_l; P_c, F_c, N_0)$ and a detailed description of the analysis of PE yield profiles are the subject of a forthcoming publication.[33]

The errors of P_c and F_c are calculated directly from the 3×3 covariance matrix $\mathbf{C}$ as

$$\sigma(x_\mu) = \sqrt{\mathbf{C}_{\mu\mu}}, \tag{11}$$

with $x_1 = P_c$, $x_2 = F_c$, and $x_3 = N_0$, under the justified assumption of uncorrelated fitting parameters. The covariance matrix **C** is computed by means of the Levenberg-Marquardt method during the minimization of

$$\chi^2 \equiv \sum_{l=1}^{P} \left(\frac{Y^{\exp}(h\nu_l) - Y^{\text{theo}}(h\nu_l; P_c, F_c; N_0)}{\sigma_l} \right)^2. \quad (12)$$

The structural parameters (P_c, F_c) presented in Sec. III consist of *value* $\langle x_\mu \rangle \pm$ *error* $\langle \delta x_\mu \rangle$. The *values* $\langle x_\mu \rangle$ are defined as

$$\langle x_\mu \rangle = \frac{1}{R} \sum_{r=1}^{R} x_{\mu r}, \quad (13)$$

with $x_{1r} = P_{cr}$ and $x_{2r} = F_{cr}$, with R being the number of separate experimental yield curves that are averaged. In order to give a conservative error estimate that accounts for both the statistical error of the PE yield as calculated by the Monte Carlo algorithm and the deviation between separate experiments (which may contain systematic errors), the *errors* $\langle \delta x_\mu \rangle$ are given by the larger of the following two quantities: the average error from the fits of the R separate experimental yield curves, using the Monte Carlo error analysis detailed in Sec. II B4a,

$$\langle \delta x_\mu \rangle_{\text{MC}} = \frac{1}{R} \sum_{r=1}^{R} \sigma(x_{\mu r}), \quad (14)$$

or the standard deviation of all $x_{\mu r}$ that contributes to the average $\langle x_\mu \rangle$,

$$\langle \delta x_\mu \rangle_{\text{std}} = \sqrt{\frac{1}{R-1} \sum_{r=1}^{R} (x_{\mu r} - \langle x_\mu \rangle)^2}; \quad (15)$$

that is, $\langle \delta x_\mu \rangle = \max(\langle \delta x_\mu \rangle_{\text{MC}}, \langle \delta x_\mu \rangle_{\text{std}})$. Note that it is not sufficient to simply quote $\langle \delta x_\mu \rangle_{\text{std}}$, for two reasons. First, often the number R of available separate experiments is small (e.g., $R < 5$); therefore $\langle \delta x_\mu \rangle_{\text{std}}$, in spite of being a useful indicator of the deviation between measured $x_{\mu r}$ values, does not provide a statistically robust measure of the actual error of $\langle x_\mu \rangle$. Second, in cases that all R measured values $x_{\mu r}$ happen to be similar, $\langle \delta x_\mu \rangle_{\text{std}}$ may turn out to be smaller than the individual $\sigma(x_{\mu r})$; in this case, $\langle \delta x_\mu \rangle_{\text{MC}}$ is a more accurate estimate of the actual error of $\langle x_\mu \rangle$.

III. EXPERIMENTAL RESULTS

A. Silver

The structural parameters of the Ag substrate atoms are obtained from two different signals, that is, the Ag3*d* PE spectrum [Fig. 5(a)] and the AgMNN Auger spectrum [Fig. 5(b)]. The former provides information regarding the bulk of the substrate, while the latter is more sensitive to the surface structure, because the kinetic energy of AgMNN Auger electrons (≈ 350 eV) is one order of magnitude smaller than that of the Ag3*d* photoelectrons ($E_k \approx 3900$ eV). Therefore, according to the universal curve of the energy-dependent escape depth d,[49] the AgMNN Auger signal probes a depth of approximately 5 Å below the surface, while the Ag3*d* PE signal is sensitive to $d \approx 20$ Å.

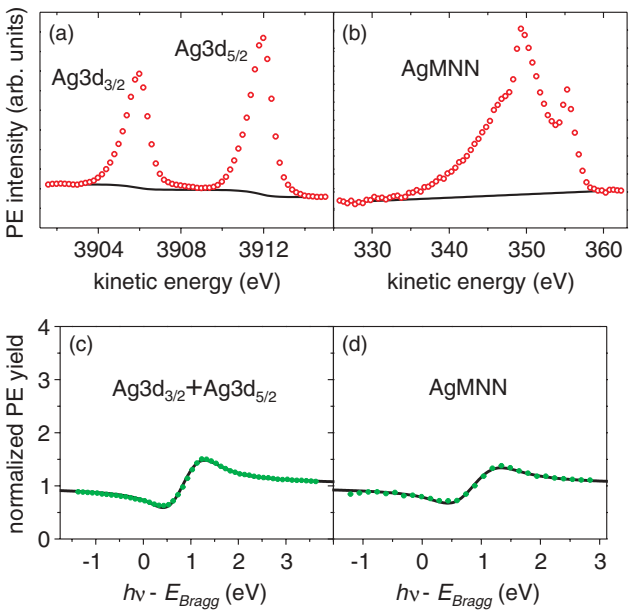

FIG. 5. (Color) (a) Ag3*d* PE spectrum. (b) AgMNN Auger spectrum. Both spectra are marked by red open circles and are measured at $h\nu = 4280$ eV. The Shirley (a) and linear (b) backgrounds are marked by a black line. (c) $\text{Ag}3d_{5/2} + \text{Ag}3d_{3/2}$ PE yield ($P_c = 0.02 \pm 0.01$, $F_c = 0.98 \pm 0.01$). The PE yield is normalized such that at photon energies away from the Bragg condition it is equal to 1. (d) AgMNN Auger electron yield ($P_c = 0.99 \pm 0.01$, $F_c = 0.83 \pm 0.02$). Experimental electron yields curves (green circles) are displayed as a function of the photon energy with respect to the Bragg energy. The corresponding fitting curves are marked by black lines.

From the analysis of the Ag3*d* PE yield profile [Fig. 5(c)] we find $P_c = 0.02 \pm 0.01$ and $F_c = 0.98 \pm 0.01$. This result confirms the perfect vertical order of bulk Ag atoms located on the (110) Bragg planes. Interestingly, the AgMNN signal, resulting from the average of two Auger yield fits [e.g., Fig. 5(d)], provides $P_c = 0.99 \pm 0.01$ and $F_c = 0.88 \pm 0.06$, with $\langle \delta x_\mu \rangle_{\text{std}}$ as the quoted error (cf. Sec. II B4b). Hence, going from the bulk to the surface-sensitive Ag PE signal, F_c decreases by 10%, in conjunction with a 3% decrease of P_c. NIXSW results thus suggest an inward relaxation of the uppermost Ag(110) surface layers. This finding is in good agreement with LEED-$I(V)$ experiments on the bare Ag(110) surface, from which an overall contraction of the first three atomic layers of $5.8 \pm 4.3\%$ of the bulk interlayer distance $d_{220} = 1.44$ Å was concluded.[50]

B. Carbon

The C1*s* PE spectrum was analyzed with the aim of determining the adsorption height of the nonequivalent carbon species of PTCDA. The high-resolution C1*s* PE spectrum measured by Schöll *et al.*[28] on a PTCDA thin film (>10 ML) adsorbed on Ag(111) (HR-mL-PE spectrum; cf. Sec. II B1) reveals the presence of four chemically different carbon atoms [Fig. 6(a)], that is, the carbon atoms of the functional groups that bond to oxygen atoms (C_1, also called C_{funct}), the carbon atoms connecting the functional groups to the perylene core (C_2), the carbon atoms of the aromatic core bonded to three other carbons (C_3), and finally the carbon atoms bonded to

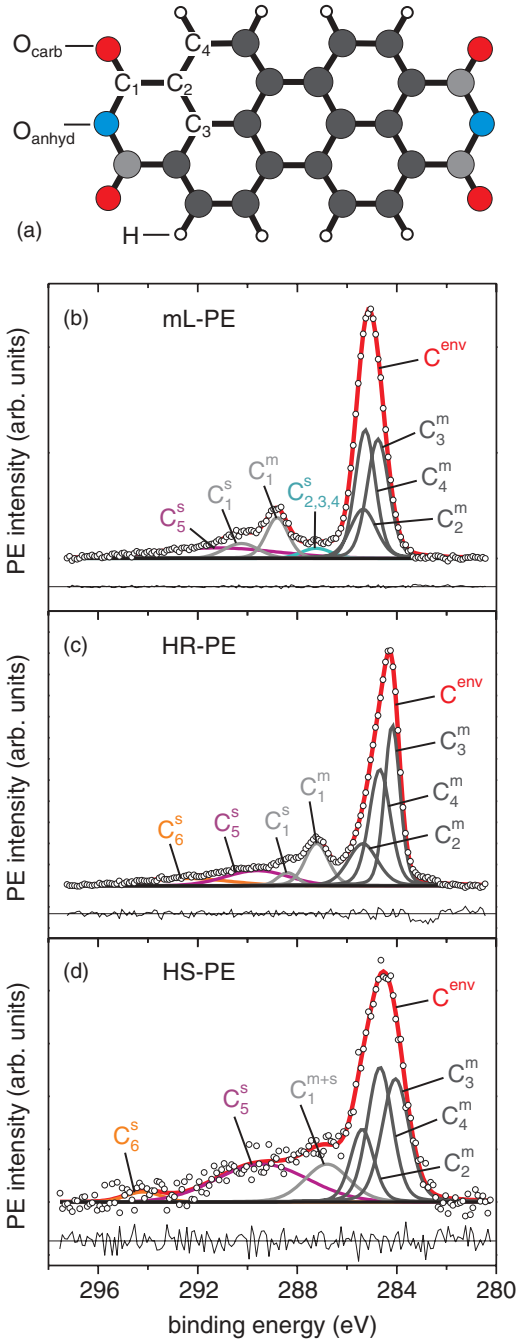

FIG. 6. (Color) (a) PTCDA molecule. (b) C1*s* mL-PE spectrum (open circles) of a PTCDA/Ag(100) multilayer ($\approx$ 40 ML), measured at the beamline ID32 (ESRF, Grenoble). (c) Sum of 26 C1*s* HR-PE spectra (open circles) of submonolayer PTCDA/Ag(110), measured with a laboratory source. (d) C1*s* HS-PE spectrum (open circles) of submonolayer PTCDA/Ag(110), measured at the beamline ID32 (ESRF, Grenoble). The acquisition settings of spectra (b)–(d) are reported in Sec. II B 1. Displayed are PE intensity (open circles); C^{env} (thick red line); C^m_2, C^m_3, C^m_4 (dark gray lines); C^m_1, C^s_1, C^{m+s}_1 (light gray lines); $C^s_{2,3,4}$ (cyan line); C^s_5 (magenta line); C^s_6 (orange line); background (straight black line); and residuals (black line below each spectrum).

hydrogen atoms (C_4). The fitting model of the HR-mL-PE spectrum reflects the stoichiometry of PTCDA, giving the following relation among the PE yields of the above mentioned carbon species:

$$Y_{C_{funct}} : Y_{C_2} : Y_{C_3} : Y_{C_4} = 4{:}4{:}8{:}8. \quad (16)$$

Because their chemical core level shifts are small, C_2, C_3, and C_4 have similar binding energies. Nevertheless, an unambiguous identification of the overlapping components was achieved by Schöll *et al.*[28] from the comparison of C1*s* PE spectra of five different π-conjugated organic molecules, including PTCDA.

The fitting model of the HR-mL-PE spectrum is transferred to the mL-PE spectrum (Sec. II B 1), fixing all peak positions with respect to C^m_4 (except for C^s_5) and constraining the relative areas of C^m_2, C^m_3, and C^m_4 according to Eq. (16). The validity of the fitting model found by Schöll *et al.*[28] is confirmed by the excellent fit of the mL-PE spectrum [Fig. 6(b)]. Therefore, in the following we use the mL-PE spectrum as our reference PTCDA multilayer spectrum. However, we note here that there are slight differences between the mL-PE spectrum and the HR-mL-PE spectrum. First, the satellite component C^s_5 at the high binding energy tail is more intense (Table II) in the mL-PE than in the HR-mL-PE spectrum.[28] This is explained by the larger number of inelastically scattered electrons in a PTCDA film that is approximately four times thicker (Sec. II B 1). Second, the FWHMs of mL-PE components (Table II) are larger than those of HR-mL-PE spectrum.

TABLE II. Overview of the binding energies (E_b), the FWHMs, the relative areas and the origins of the the fitting components shown in Figs. 6(b)–6(d). Sat refers to satellite peaks that could not be further specified.

Peak	E_b (eV)	FWHM (eV)	Area (%)	Origin
	Multilayer PTCDA/Ag(100) (mL-PE)			
C^m_3	284.76	1.03	27.91	C_{peryl}
C^m_4	285.27	0.96	27.91	
C^m_2	285.35	1.25	13.96	
$C^s_{2,3,4}$	287.24	1.40	2.92	
C^m_1	288.81	1.06	9.74	C_{funct}
C^s_1	290.25	1.64	5.02	
C^s_5	291.24	5.81	12.54	Sat
	Submonolayer PTCDA/Ag(110) (HR-PE)			
C^m_3	284.18	1.01	27.93	C_{peryl}
C^m_4	284.68	0.73	27.93	
C^m_2	285.36	1.40	13.97	
C^m_1	287.21	1.11	11.21	C_{funct}
C^s_1	288.39	0.95	2.66	
C^s_5	289.60	2.98	9.69	Sat
C^s_6	292.48	4.18	6.61	
	Submonolayer PTCDA/Ag(110) (HS-PE)			
C^m_3	284.05	1.30	24.77	C_{peryl}
C^m_4	284.68	1.19	24.77	
C^m_2	285.39	1.10	12.39	
C^{m+s}_1	286.80	2.10	12.36	C_{funct}
C^s_5	289.41	4.35	23.26	Sat
C^s_6	294.18	1.73	2.45	

This is because of the lower signal-to-noise ratio due to the smaller C1s photoionization cross section for $h\nu = 3024$ eV (mL-PE spectrum; Sec. II B1) as compared to $h\nu = 335$ eV (HR-mL-PE spectrum).[28]

In comparison with the perylene core carbon atoms ($C_{peryl} = C_2 + C_3 + C_4$), C_{funct} has approximately 3 eV larger binding energy [Fig. 6(b); Table II]. This can be rationalized by the following initial-state picture. The highly electronegative oxygen atoms withdraw electrons, thereby reducing the charge density at the C_{funct} carbons, hence inducing a significant C1s chemical shift at these carbons towards higher binding energy. Since the fitting model described above refers to a PE spectrum measured on approximately 40 PTCDA layers, it is representative of PTCDA molecules within the film. When PTCDA is in direct contact with the metal substrate, a redistribution of the C1s PE intensity due to chemisorption and substantially different intermolecular interactions is expected.

In Fig. 6(c) we report a C1s HR-PE spectrum measured on a PTCDA/Ag(110) submonolayer (Sec. II B1). It has been decomposed into four main components C_1^m, C_2^m, C_3^m, and C_4^m and three satellite peaks C_1^s, C_5^s, and C_6^s. The most notable difference compared to the spectrum measured on a PTCDA thin film in Fig. 6(b) is the smaller chemical shift of C_1^m. We explain this with the additional bonding of carboxylic oxygen with the surface, which leads to a weakening of the C=O bond and thus leaves C_1 carbons in a different chemical environment. Furthermore, because of the lack of evidence for the satellite peak of C_2^m, C_3^m, C_4^m, that is, $C_{2,3,4}^s$ in the spectrum of Fig. 6(b), we account for its PE intensity by means of a larger FWHM of C_2^m (Table II). In the high binding energy tail of the spectrum two additional satellite components, C_5^s and C_6^s, are introduced. Since the satellite structure is related to the reaction of the molecule to the creation of a core hole, the larger intensity of $C_5^s + C_6^s$ as compared to C_5^s in Fig. 6(b) is ascribed to a modified electronic structure at the molecule-metal interface and to a different molecule-molecule interaction.[28]

Due to the higher photon energy employed in the NIXSW experiments on Ag(110) (4280 eV) and the consequently lower C1s photoionization cross section and due to instrumental limitation of the PHI electron analyzer at beamline ID32 at the ESRF, HS-PE spectra [Fig. 6(d)], measured on the same sample on which NIXSW experiments were performed (see Sec. II B1), exhibit a lower resolution than HR-PE submonolayer spectra [Fig. 6(c)] recorded with the Scienta R4000 with monochromated Al $K\alpha$ excitation and discussed above. However, on the basis of the mL-PE spectrum in Fig. 6(b) and the submonolayer HR-PE spectrum in Fig. 6(c) the following fitting model, shown in Fig. 6(d), has been developed. This model provides a higher coherent fraction F_c than alternative ones that we have tested; therefore, it was used for fitting all C1s XSW-PE spectra. It has the following features: Because the low spectral resolution and signal-to-noise ratio prevent C_1^s from being clearly discernible, a broader C_1^{m+s} component accounts for the weak C_1^s peak and the stronger C_1^m peak; the latter mainly determines the position of the C_1^{m+s} peak. Similarly, the satellite peaks of C_2^m, C_3^m, C_4^m are included into C_2^m that is shifted to higher binding energy, as in the HR-PE spectrum [Fig. 6(c)]. The relative areas of C_2^m, C_3^m, and C_4^m are fixed according to Eq. (16), while the corresponding relative FWHMs are constrained as in the HR-mL-PE spectrum[28] (Table II). These are the only constraints employed in fitting the C1s spectrum in Fig. 6(d). As a result of the fit, the PE yields $Y_{C_2^m}$, $Y_{C_3^m}$, $Y_{C_4^m}$, and $Y_{C_1^{m+s}}$ fulfill Eq. (16).

TABLE III. Coherent position P_c, corresponding adsorption height d_c (Å) [calculated as $(1 + P_c) \times d_{Ag(220)}$, with $d_{Ag(220)} = 1.44$ Å] and coherent fraction F_c of C^{env}, $C_2^m + C_3^m + C_4^m$ ($= C_{peryl}^m$), C_1^{m+s} ($= C_{funct}^m$), C_5^s, O^{env}, $O_{carb}^m + O_{carb}^s$, $O_{anhyd}^m + O_{anhyd}^s$, all measured on a PTCDA/Ag(110) submonolayer. Carbon values are an average of two NIXSW data sets, while oxygen values are an average of three NIXSW data sets. Quoted error bars are $\delta x_\mu = \max(\langle \delta x_\mu \rangle_{MC}, \langle \delta x_\mu \rangle_{std})$ (cf. Sec. 4). Results reported here are identical within the error bars with those quoted in Ref. 20. Small differences are assigned to the slightly different fitting models and the different analysis programs, that is, TORRICELLI (Refs. 31–33) and XSWAVES (Ref. 34).

	P_c	d_c(Å)	F_c
C^{env}	0.77 ± 0.01	2.56 ± 0.02	0.40 ± 0.04
$C_2^m + C_3^m + C_4^m$	0.79 ± 0.01	2.59 ± 0.01	0.40 ± 0.06
C_1^{m+s}	0.70 ± 0.08	2.45 ± 0.11	0.44 ± 0.08
C_5^s	0.77 ± 0.03	2.56 ± 0.04	0.39 ± 0.08
O^{env}	0.64 ± 0.03	2.36 ± 0.05	0.25 ± 0.05
$O_{carb}^m + O_{carb}^s$	0.60 ± 0.04	2.32 ± 0.05	0.21 ± 0.04
$O_{anhyd}^m + O_{anhyd}^s$	0.67 ± 0.04	2.41 ± 0.06	0.34 ± 0.09

The structural parameters for the various C1s components are compiled in Table III. Two experiments have been performed on the same sample preparation and the PE yields of one of those are reported as examples in Figs. 7(a)–7(c). By construction, the PE yield profiles of C_2^m, C_3^m, and C_4^m are the same; therefore, only their sum C_{peryl}^m ($= C_2^m + C_3^m + C_4^m$) is considered [Fig. 7(a); Table III]. The corresponding $P_c = 0.79 \pm 0.01$ with $F_c = 0.40 \pm 0.06$ gives an average adsorption height of the perylene carbons of 2.59 ± 0.01 Å. Here $\langle \delta P_c \rangle_{MC}$ is quoted as error for the coherent position, while $\langle \delta F_c \rangle_{std}$ is quoted for the coherent fraction (cf. Sec. II B4b).

For C_{funct}^m ($= C_1^{m+s}$), the fitting results of the two experimental data sets are $P_c = 0.75 \pm 0.03$ and $P_c = 0.64 \pm 0.04$ [Fig. 7(b)]. In this case, the deviation between the two independent measurements on the same sample preparation is larger than the statistical error of each fit separately. Therefore, the standard deviation $\langle \delta P_c \rangle_{std}$ is quoted as the error of C_{funct}^m in Table III. Note that in both experimental data sets the functional carbons are below the perylene core. The average C_{funct} adsorption height of 2.45 ± 0.11 Å is 0.14 Å smaller than that of C_{peryl}. Notably, for C_{funct} the coherent fraction $F_c = 0.44 \pm 0.08$ is slightly larger than that of C_{peryl}. This F_c results from the average of the two experimental values, 0.42 ± 0.07 and 0.45 ± 0.09.

C_5^s is introduced as a satellite component and is expected to include contributions from carbon atoms of the perylene core and of the functional group. The sum of the respective Argand vectors, weighted with the corresponding PE yield intensities [Eq. (16)], that is, $5 \times Y_{C_{peryl}^m} + Y_{C_{funct}^m}$, coincides with the P_c and F_c values derived from the fitting of the C_5^s yield profiles [Fig. 7(c)]. For the coherent position P_c and the coherent fraction F_c of C_5^s $\langle \delta P_c \rangle_{MC}$ and $\langle \delta F_c \rangle_{MC}$ are quoted in Table III. Note that larger error bars of C_1^{m+s} and C_5^s [Figs. 7(b) and 7(c)] compared to those of $C_2^m + C_3^m + C_4^m$ [Fig. 7(a)] follow from the smaller signal-to-noise ratio, as it is evident

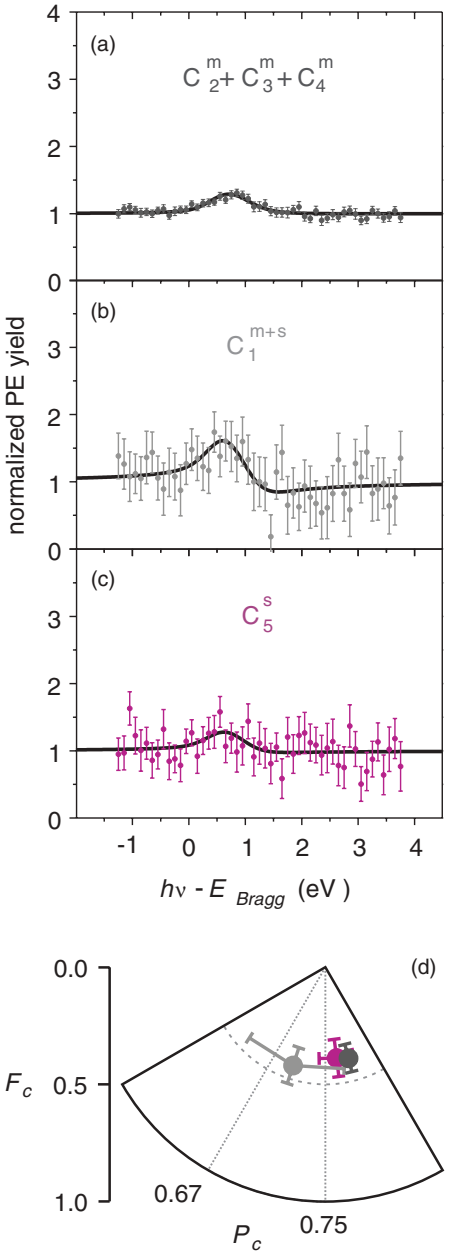

FIG. 7. (Color) PE yield of $C_2^m + C_3^m + C_4^m$ [(a) dark gray circles, $P_c = 0.79 \pm 0.01$, $F_c = 0.35 \pm 0.02$], C_1^{m+s} [(b) light gray circles, $P_c = 0.64 \pm 0.04$, $F_c = 0.45 \pm 0.09$], and C_5^s [(c) magenta circles, $P_c = 0.77 \pm 0.03$, $F_c = 0.41 \pm 0.09$] corresponding to one NIXSW data set, with the fitting curves marked in black. The PE yield is normalized such that at photon energies away from the Bragg condition it is equal to 1. (d) Argand diagram (P_c, F_c) of $C_2^m + C_3^m + C_4^m$, C_1^{m+s}, and C_5^s corresponding to the average over the two NIXSW data sets.

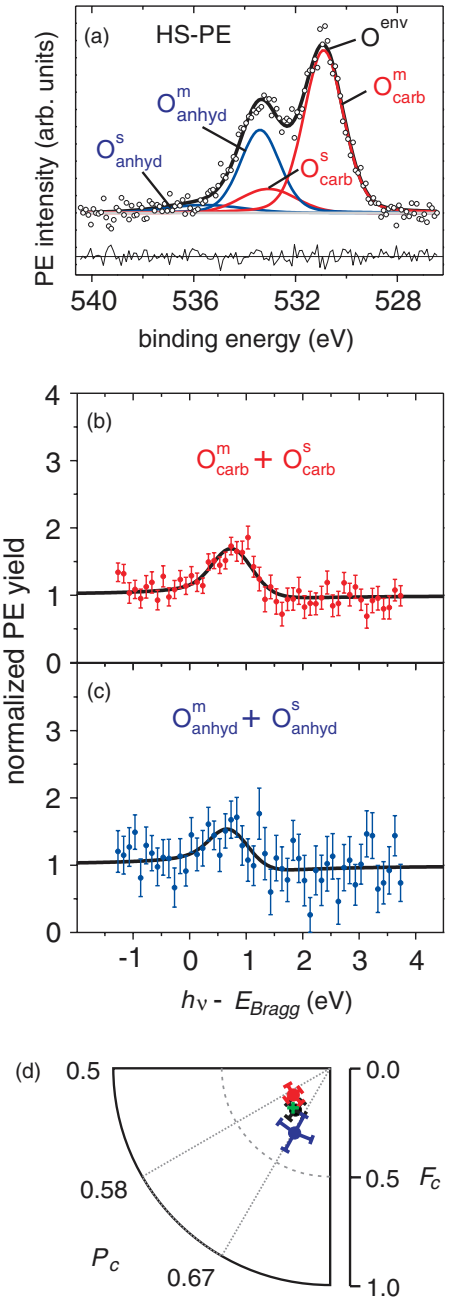

FIG. 8. (Color) (a) O1*s* HS-PE spectrum (open circles) of submonolayer PTCDA/Ag(110) measured at the beamline ID32 (ESRF, Grenoble) with the acquisition settings reported in Sec. II B 1. Displayed are $O^{env} = O^m_{carb} + O^s_{carb} + O^m_{anhyd} + O^s_{anhyd}$ (black line), O^m_{carb} and O^s_{carb} (red lines), O^m_{anhyd} and O^s_{anhyd} (blue lines), background (gray line), and residuals (black line below the spectrum). (b) $O^m_{carb} + O^s_{carb}$ PE yield (red circles). (c) $O^m_{anhyd} + O^s_{anhyd}$ PE yield (blue circles). The fitting curves of the PE yields are marked in black. The PE yield is normalized such that at photon energies away from the Bragg condition it is equal to 1. (d) Argand diagram (P_c, F_c) of $O^m_{carb} + O^s_{carb}$ (red circle), $O^m_{anhyd} + O^s_{anhyd}$ (blue circle), O^{env} (black circle) corresponding to the average over three NIXSW data sets, plus the weighted sum of O_{carb} and O_{anhyd} (P_c, F_c) (green +; see text).

from the HS-PE spectrum in Fig. 6(d). Finally, due to the very low signal-to-noise ratio C_6^s provides a PE yield profile that does not carry any structural information.

C. Oxygen

The O1*s* HS-PE spectrum of PTCDA [Fig. 8(a)] consists of two peaks that are chemically shifted by approximately 2.5 eV with respect to each other. These two peaks represent O atoms in two different chemical environments, that is, carboxylic oxygen O_{carb} that is doubly bonded to one C_{funct} carbon and anhydride oxygen O_{anhyd} that is singly bonded to two C_{funct}

TABLE IV. Overview of the binding energies (E_b), the FWHMs, the relative areas and the origins of the fitting components shown in Fig. 8(a).

Peak	E_b (eV)	FWHM (eV)	Area (%)	Origin
	Submonolayer PTCDA/Ag(110) (HS-PE)			
O^{m}_{carb}	530.90	1.84	55.97	O_{carb}
O^{s}_{carb}	533.07	2.60	10.64	
O^{m}_{anhyd}	533.40	1.84	28.54	O_{anhyd}
O^{s}_{anhyd}	535.60	3.63	4.85	

carbons. PTCDA molecules have four O_{carb} and two O_{anhyd} atoms. Therefore, in first approximation, the most intense PE peak at higher binding energy is assigned to O_{carb}, while the less intense one at lower binding energy is assigned to O_{anhyd}. The fitting model of the O1*s* PE spectrum consists of two main components O^{m}_{carb} and O^{m}_{anhyd} and two corresponding satellites O^{s}_{carb} and O^{s}_{anhyd}. In this model, O^{s}_{carb} and O^{s}_{anhyd} are fixed at a distance of 2.17 and 2.20 eV, respectively, from their main peaks, with their PE yield fixed to 19% and 17% of the respective main component (Table IV). The FWHMs of O^{m}_{carb} and O^{m}_{anhyd} are set to be identical. Given these constraints, the PE yield of the fitting components reflect the correct stoichiometry ratio $[Y_{O^{m}_{carb}} + Y_{O^{s}_{carb}}] : [Y_{O^{m}_{anhyd}} + Y_{O^{s}_{anhyd}}] = 2{:}1$.

In comparison with the O1*s* HR-mL-PE spectrum measured on a 10-layer PTCDA thin film by Schöll *et al.*[28] and with the O1*s* multilayer PTCDA/Ag(100) spectrum (not shown here), O^{m}_{anhyd} is found at the same binding energy, while O^{m}_{carb} is at approximately 0.75 eV lower binding energy. The binding energy shift of O^{m}_{carb} and of both satellite components is assigned to the O-Ag interaction that leads to a distortion of the PTCDA functional groups (see below), to the screening of the core electrons by the metallic substrate, and to the different intermolecular interactions of PTCDA in the submonolayer compared to the multilayer.

The O1*s* fitting model described above and detailed in Table IV is used to fit three NIXSW data sets measured on the same submonolayer PTCDA/Ag(110) preparation. The energy position and the FWHM of each component are kept fixed to the values derived from the HS-PE spectra. Only the PE yields are left free, with the constraint that $Y_{O^{s}_{carb}}/Y_{O^{m}_{carb}}$ and $Y_{O^{s}_{anhyd}}/Y_{O^{m}_{anhyd}}$ are fixed to the values derived from the HS-PE spectrum in Fig. 8(a).

Figures 8(b) and 8(c) show the fits of one of the three data sets. The average results of the three NIXSW data sets provide O_{carb} at 2.32 ± 0.05 Å with $F_c = 0.21 \pm 0.04$, while O_{anhyd} are found at 2.41 ± 0.06 Å with $F_c = 0.34 \pm 0.09$ (Table III). For O_{carb}, $\langle \delta P_c \rangle_{std} = \langle \delta P_c \rangle_{MC}$ and $\langle \delta F_c \rangle_{std} = \langle \delta F_c \rangle_{MC}$ are quoted as errors, whereas the quoted errors for O_{anhyd} are $\langle \delta P_c \rangle_{MC}$ and $\langle \delta F_c \rangle_{MC}$ (cf. Sec. II B4b).

Finally, to verify the self-consistency of the fitting model, O_{carb} (red) and O_{anhyd} (blue) vectors in the Argand diagram in Fig. 8 are summed with their respective weights as given by the molecular stoichiometry. The sum vector (green) coincides with the Argand vector of O^{env}, as expected. This confirms that the peak assignments of our fitting model are consistent with the stoichiometry of PTCDA.

IV. DISCUSSION

We have shown in Sec. III that a careful analysis of C1*s* and O1*s* PE spectra allows the adsorption height of atoms in different chemical environments with a sufficiently large chemical shifts to be determined. On the basis of the resulting structural parameters (P_c, F_c) and the corresponding error estimates we now turn to the discussion of the adsorption geometry of PTCDA on Ag(110) (Sec. IV A). Possible reasons for the rather low coherent fractions are critically discussed in Sec. IV B. Finally, in Sec. IV C NIXSW structural data are compared to *ab initio* calculations and a bonding mechanism of PTCDA on Ag(110) is proposed.

A. PTCDA adsorption geometry on Ag(110)

Figure 9(b) displays the archlike geometry of PTCDA on Ag(110) with the functional groups bent towards the surface. Carboxylic (anhydride) O atoms are at 2.32 Å (2.41 Å) from the surface Bragg plane, hence 0.27 Å (0.18 Å) below the carbon perylene core (C_{peryl}) of PTCDA [Fig. 9(a)]. In agreement with a smaller adsorption height of O atoms, C atoms of the functional groups, that is, C_{funct}, are also located 0.14 Å below C_{peryl}, as illustrated in Fig. 9(a).

To discuss the interaction of PTCDA molecules with the Ag(110) surface, we focus on the interatomic distances d_i (X-Ag) between the atoms X = C,O and the nearest Ag

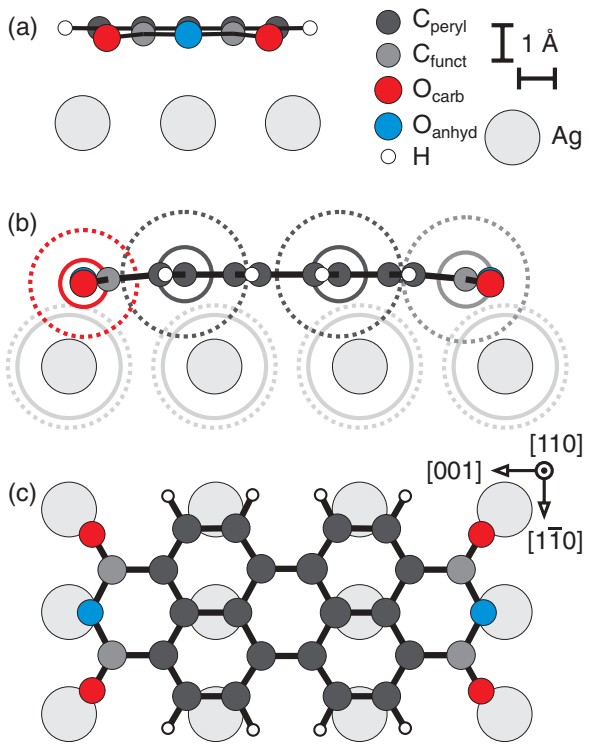

FIG. 9. (Color) (a) Side view (along the long molecular axis) of PTCDA/Ag(110). (b) Side view (along the short molecular axis) of PTCDA/Ag(110). (c) Top view of PTCDA/Ag(110). Solid circles indicate the atomic positions. In panel (b), solid lines indicate covalent radii (Ref. 54) ($r^{C}_{cov} = 0.73$ Å, $r^{O}_{cov} = 0.66$ Å, $r^{Ag}_{cov} = 1.45$ Å) and dotted lines indicate van der Waals radii (Ref. 55) ($r^{C}_{vdW} = 1.75$ Å, $r^{O}_{vdW} = 1.50$ Å, $r^{Ag}_{vdW} = 1.72$ Å).

surface atoms, because they can be directly compared with the corresponding van der Waals (vdW) and covalent (cov) bond lengths. To calculate d_i (X-Ag), the lateral position of PTCDA with respect to the Ag(110) substrate must be known. The orientation of PTCDA within the brick-wall unit cell [Fig. 2(b)] and its position relative to the Ag substrate [Fig. 9(c)] are revealed by STM experiments.[17,51] PTCDA is oriented with the long axis parallel to the [001] direction. Its center is located between the closed-packed Ag rows, as shown in Fig. 9(c). d_i(O-Ag) and d_i(C-Ag) are estimated on the basis of the vertical positions of PTCDA from NIXSW and lateral positions (gas phase) from GAUSSIAN03[52] calculations,[53] respectively, subject to the assumption of an unrelaxed topmost Ag layer that coincides with the surface Bragg plane.

Remarkably, $d_i(\mathrm{O_{carb}\text{-}Ag}) = d_i(\mathrm{O_{anhyd}\text{-}Ag}) = 2.45$ Å, despite the different chemical environments of $\mathrm{O_{carb}}$ and $\mathrm{O_{anhyd}}$ within the molecule. This finding suggests a strong interaction of PTCDA functional groups with Ag substrate atoms, which distorts the gas-phase planar geometry and leads to the formation of covalent O-Ag bonds. To better asses the molecule-metal interaction, $d_i(X\text{-Ag})$ are compared with the corresponding sum of vdW radii $r^{\mathrm{X}}_{vdW} + r^{\mathrm{Ag}}_{vdW}$ and the sum of covalent radii $r^{\mathrm{X}}_{cov} + r^{\mathrm{Ag}}_{cov}$. The average distance $\langle d_i(\mathrm{O\text{-}Ag})\rangle = [2 \times d_i(\mathrm{O_{carb}\text{-}Ag}) + d_i(\mathrm{O_{anhyd}\text{-}Ag})]/3 = 2.45$ Å is 16% larger than the corresponding sum of covalent radii $r^{\mathrm{O}}_{cov} + r^{\mathrm{Ag}}_{cov} = 2.11$ Å, while the average distance $\langle d_i(\mathrm{C\text{-}Ag})\rangle = [20 \times d_i(\mathrm{C_{peryl}\text{-}Ag}) + 4 \times d_i(\mathrm{C_{funct}\text{-}Ag})]/24 = 2.92$ Å is 16% smaller than the corresponding sum of vdW radii $r^{\mathrm{C}}_{vdW} + r^{\mathrm{Ag}}_{vdW} = 3.47$ Å. This shows that, on the one hand, the distance of PTCDA oxygen atoms from Ag atoms is 0.34 Å above the lower limit of the covalent bond length, while, on the other hand, the average distance of PTCDA carbon atoms from Ag atoms is 0.55 Å below the upper limit of the vdW interaction length, as shown in Fig. 9(b). Both facts are consistent with a significant chemical contribution to the interaction between the PTCDA molecule and the Ag(110) substrate, which bends the molecular plane in order to favor the interaction of the functional groups oxygen atoms with the Ag surface atoms underneath and brings the perylene core into the Pauli repulsion limit.[20]

B. Interpretation of PTCDA coherent fraction

As mentioned in Sec. II B 1, the coherent fraction F_c can only take values between 0 and 1. Small F_c values can arise from static or dynamic disorder, for example, multiple site occupation or molecular vibrations. In the present NIXSW experiments the measured F_c values of each atomic species are lower than 0.5. In this section we discuss some of the possible reasons for such low coherent fractions.

1. *Effect of the Bragg spacing*

F_c is related to the vertical distribution of atoms within one Bragg spacing d_{hkl}. Hence, its value scales with d_{hkl}, which in turn depends on the Bragg plane orientation (hkl) and on the substrate element itself. The reason for the dependance of F_c on d_{hkl} is explained as follows.

Consider N adsorbate atoms of the same chemical species X ($X = C, O, \ldots$), labeled X_i for $i = 1, \ldots, N$. Assume their chemical shifts are so small that they cannot be resolved in XPS. Only one set of structural parameters (P_c, F_c) can then be extracted. The normalized distribution function of the atomic positions d^{X_i} is

$$f^X(z) = \frac{1}{N}\sum_{i=1}^{N}\delta(z - d^{X_i}). \tag{17}$$

In an NIXSW experiment the Fourier transform of the distribution $f^X(z)$, that is,

$$\tilde{f}^X_{\mathbf{H}} = \int_0^{d_{hkl}} f^X(z)\exp\left(2\pi i\frac{z}{d_{hkl}}\right)dz, \tag{18}$$

is measured, where $\mathbf{H}$ is the reciprocal lattice vector corresponding to the (hkl) lattice plane at which the incoming x-ray beam is reflected. As a complex quantity, the Fourier transform can be expressed as

$$\tilde{f}^X_{\mathbf{H}} = \mathrm{Re}\,\tilde{f}^X_{\mathbf{H}} + i\,\mathrm{Im}\,\tilde{f}^X_{\mathbf{H}} = F^X_c\exp\left(2\pi i P^X_c\right), \tag{19}$$

where F^X_c is the coherent fraction and P^X_c is the coherent position corresponding to the distribution $f^X(z)$. Hence, F^X_c can be expressed as

$$F^X_c = \sqrt{\left[\mathrm{Re}\,\tilde{f}^X_{\mathbf{H}}\right]^2 + \left[\mathrm{Im}\,\tilde{f}^X_{\mathbf{H}}\right]^2}. \tag{20}$$

Inserting Eq. (17) into Eq. (18), it follows that

$$\tilde{f}^X_{\mathbf{H}} = \sum_{i=1}^{N} F^{X_i}_c\exp\left(2\pi i P^{X_i}_c\right), \tag{21}$$

where $F^{X_i}_c = 1/N$ and $P^{X_i}_c = d^{X_i}_c/d_{hkl}$. From Eqs. (19) and (21), we obtain

$$\mathrm{Re}\,\tilde{f}^X_{\mathbf{H}} = \sum_{i=1}^{N} 1/N\cos\left(2\pi\frac{d^{X_i}_c}{d_{hkl}}\right), \tag{22}$$

$$\mathrm{Im}\,\tilde{f}^X_{\mathbf{H}} = \sum_{i=1}^{N} 1/N\sin\left(2\pi\frac{d^{X_i}_c}{d_{hkl}}\right). \tag{23}$$

Therefore, given the distribution $f^X(z)$ of fixed width in z with atoms at fixed positions d^{X_i}, as the period $d_{hkl}/2\pi$ of the cosine and sine functions decreases, $\mathrm{Re}\,\tilde{f}^X_{\mathbf{H}}$ and $\mathrm{Im}\,\tilde{f}^X_{\mathbf{H}}$ will also decrease. This will lead to a smaller coherent fraction F^X_c. In general, for a distribution $f^X(z)$, with $(\max(d^{X_i}) - \min(d^{X_i})) < d_{hkl}$, the lower d_{hkl} is, the lower F_c will be.

In order to estimate the effect of the Bragg spacing on F_c, we compare the three canonical low index Ag surfaces, that is, (111), (100), and (110), with $d_{\mathrm{Ag(111)}} = 2.36$ Å, $d_{\mathrm{Ag(200)}} = 2.04$ Å, and $d_{\mathrm{Ag(220)}} = 1.44$ Å. Note that (100) and (110) reflections have vanishing intensity because the corresponding structure factors are zero.[26] (200) and (220) are the lowest order reflections with nonvanishing intensity. Assume we have a vertical distance of 0.20 Å between two atoms X_i adsorbed on each of the three Ag surfaces. The decrease of the coherent fraction, compared to the scenario in which both atoms are at the same vertical position, is 3%, 5%, and 10% on Ag(111), Ag(100), and Ag(110), respectively. Therefore, the lower F_c of PTCDA/Ag(110) as compared to PTCDA/Ag(111)[6] is partially due to the smaller $d_{\mathrm{Ag(220)}}$.

2. *Effect of molecular vibrations*

Molecular vibrations can affect NIXSW structural parameters, because the PE process and the associated electronic relaxation occur on a time scale of $\sim 10^{-15}$ s, while the nuclear motion associated to low frequency vibrations is approximately two orders of magnitude slower, in the range of $\sim 10^{-13}$ s. The Born-Oppenheimer approximation is thus valid for the XPS and NIXSW experiments.[56] However, molecular vibrations can only partially explain the significant reduction in the coherent fraction.[57] In fact, an atomic vertical displacement of ± 0.10 Å from its equilibrium position corresponds to a F_c decrease of only 10% on Ag(110) (Sec. IV B 1). This estimate suggests that other phenomena, for example, molecular diffusion (Sec. IV B 3), may contribute to further increase the vertical disorder of the PTCDA submonolayer on Ag(110).

3. *Effect of molecular diffusion on F_c*

STM experiments proved the presence of diffusing PTCDA molecules between PTCDA islands adsorbed on the Ag(100) surface, on the basis of tunneling current pulses that are absent on the bare substrate.[58] The corresponding diffusion constant was found to be 4.0×10^3 nm^2 s^{-1} (Ref. 59). Moreover, the decay of PTCDA islands on Ag(100) was found to be diffusion limited; that is, the diffusion rate of molecules from or to the islands is smaller than the attachment-detachment rate. As a consequence, molecules distribute only slowly and with a nonconstant density on the surface. In particular, coverages between $\Theta = 0.0004$ and 0.02 were measured between the PTCDA islands, with higher coverages near an island. These values correspond to coverages between 0.4% and 20% of the overall PTCDA coverage of that experiment (0.10 ML) and to molecular densities between $\rho = 3.1 \times 10^{-4}$ nm^{-2} and $\rho = 1.5 \times 10^{-2}$ nm^{-2}. Therefore, a significant amount of molecules diffusing on the surface can have undefined positions with unknown adsorption geometries.

An analogous island decay mechanism is expected for PTCDA/Ag(110) due to the similarities with PTCDA/Ag(100). The experimental evidence for this is given by an STM study of submonolayer PTCDA/Ag(110) (Ref. 60), which shows static molecular islands at 50 K, while at 295 K repeated STM images of the same surface area reveal the growth of larger islands at the expense of the smaller ones. This significant rearrangement of islands on the surface implies the presence of a 2D gas of mobile molecules at 295 K. Furthermore, the presence of occasional streaks of apparent height equal to that of PTCDA islands is observed with a larger density in the proximity of an island than on open terraces. This evidence strongly supports the diffusion-limited decay of PTCDA islands[61] on Ag(110) as well. The presence of PTCDA in a 2D gas phase diffusing on the surface can partially rationalize the relatively low coherent fraction of PTCDA/Ag(110): If molecules diffusing on the surface have different vertical positions with on average $F_c = 0$, then they contribute to a decrease of the overall coherent fraction of the molecular layer without affecting the height d_c of coherently adsorbed molecules forming the ordered islands.

TABLE V. Adsorption heights of C_{peryl}, C_{funct}, O_{carb}, and O_{anhyd} atoms, with respect to the topmost unrelaxed Ag layer, obtained from NIXSW experiments, MP2 calculations (Ref. 62) and DFT calculations (Ref. 20). ΔC and ΔO are the differences between nonequivalent C and O species, respectively. Δ are the percentage deviations of theoretical values from the experimental ones. Experimental results reported here are identical within the error bars with those quoted in Ref. 20. Small differences are assigned to the slightly different fitting models and the different analysis programs, that is, TORRICELLI (Refs. 31–33) and XSWAVES (Ref. 34).

	NIXSW	MP2	Δ(%)	DFT	Δ(%)
C_{peryl}	2.59 ± 0.01	2.69	+4	2.71	+5
C_{funct}	2.45 ± 0.11	2.64	+8	2.53	+3
ΔC	0.14 ± 0.12	0.05	−64	0.18	+29
O_{carb}	2.32 ± 0.05	2.50	+8	2.38	+3
O_{anhyd}	2.41 ± 0.06	2.63	+9	2.46	+2
ΔO	0.09 ± 0.11	0.13	+44	0.08	−11

C. Comparison of NIXSW data with *ab initio* calculations

The general trend of PTCDA/Ag(110) adsorption heights resulting from NIXSW experiments is well reproduced by second-order Møller-Plesset theoretical calculations (MP2) of a single PTCDA molecule adsorbed on a two-layer slab of 32 Ag atoms.[62] Theoretical and experimental results are reported and compared in Table V. In particular, the perylene core, that is, the larger portion of the molecule, is predicted by MP2 calculations to adsorb only 4% (0.10 Å) higher than in experiment. This represents a good agreement, if we consider that, due to the computationally expensive calculations, only a significantly reduced substrate slab is taken into account. In contrast, MP2 theory overestimates the adsorption height of the anhydride functional groups, by approximately 8% (0.20 Å). Although the calculations predict a flatter adsorption geometry than found in experiment, the main features of the adsorbed molecules, that is, the downward bending of the molecule with C_{funct} beneath C_{peryl} and O_{carb} beneath O_{anhyd}, are correctly reproduced.

An even more accurate prediction, with deviations from NIXSW data smaller than 5%, is provided by density functional theory (DFT) calculations with the PBE functional[63] in combination with the empirical dispersion correction D3(BJ).[20,64,65] The silver surface is modeled by a (3 2 | −3 2) supercell consisting of seven layers, with the Ag atoms of the two bottom layers fixed to their ideal bulk positions during the structural optimization process. One PTCDA molecule per unit cell was considered as in the brick-wall phase [Fig. 2(b)]. Although DFT slightly overestimates all the adsorption heights, the internal distortion of PTCDA is satisfactorily reproduced, with O_{carb} closest to the Ag surface, followed by O_{anhyd}, C_{funct}, and C_{peryl}.

Having proved the good agreement between DFT and NIXSW results, as far as the structure is concerned, we turn to discuss the electronic properties of the PTCDA/Ag(110) interface. The electron density maps of the PTCDA/Ag(110) interface shown in Ref. 20 reveal the accumulation of charge in two regions: (a) between $O_{carb/anhyd}$ and the respective Ag atoms underneath and (b) below those C_{peryl} atoms that are located at the long edges of the PTCDA molecule. Finding

(a) corroborates our NIXSW-based conjecture of the existence of O-Ag chemical bonds. Finding (b) indicates the formation of a weak covalent/coordinative bond between the outer C_{peryl} atoms and Ag surface atoms. In contrast, the low electron density below the central axis of the PTCDA molecule suggests a stronger Pauli repulsion between the C_{peryl} atoms and the substrate in that region. This interpretation of the electronic charge distribution is consistent with the buckling of the surface. In particular, according to DFT calculations,[20] the two Ag atomic rows beneath the long edges of the PTCDA molecule are pulled upwards in comparison with the bulk truncated structure, while the Ag atomic row beneath the central axis of PTCDA is pushed downwards. The former is a consequence of the weak chemical/coordinative C_{peryl}-Ag bond, while the latter is an effect of the stronger Pauli repulsion below the central axis as compared to the outer edges of the perylene core.

Finally, we discuss the bonding mechanism of PTCDA on Ag(110) on the basis of experimental and theoretical results to date. UPS experiments[18] and *ab initio* calculations[20,62] show that upon adsorption on the Ag(110) surface the former lowest unoccupied molecular orbital (LUMO) of the free molecule becomes occupied. As a consequence of the charge transfer to the LUMO, bond lengths where the LUMO has antinodes shorten and the bond order increases, while bond lengths where the LUMO has nodes elongate and the bond order decreases.[20,66] In particular, the LUMO of PTCDA has a node at the C=O double bond which is thus expected to be elongated and weakened. This in turn aids the formation of O-Ag bonds bearing a significant chemical character, as suggested by present NIXSW results, supported by calculations[20,62] and previous HREELS measurements.[67,68] In particular, the latter reveal a shift of the C=O stretch mode in going from multilayer to submonolayer PTCDA/Ag(110), which we assign to the formation of O_{carb}-Ag bonds. The bonding of the functional groups tends to pull the PTCDA closer to the surface at a distance where Pauli repulsion between filled molecular and substrate orbitals becomes significant. As a result of the delicate balance between charge transfer, O-Ag covalent bonds, C-Ag chemical interaction, long-range dispersive interactions and local Pauli repulsion PTCDA adopts the downward bent archlike geometry unveiled by NIXSW. In fact, the smaller F_c of C_{peryl} (0.40) compared to C_{funct} (0.44) suggests an even further distortion of the carbon backbone, which, however, cannot yet be resolved with the present instrumentation.

V. CONCLUSIONS

In this work, NIXSW data of a submonolayer of PTCDA molecules adsorbed on the Ag(110) surface were presented, analyzed, and discussed. Special emphasis was placed on the differential analysis of different oxygen and carbon species within the molecule, in an attempt to reveal the structure of the adsorbed PTCDA in as much detail as possible. In order to assess the significance of the structural parameters P_c and F_c, a systematic and careful error analysis was performed. According to the resulting structural model, PTCDA adsorbs in an archlike geometry with the functional groups bent towards the surface. It was demonstrated that this experimentally determined adsorption geometry provides the key to our understanding of the bonding of PTCDA on Ag(110). In particular, from the adsorption geometry of PTCDA a chemical contribution to the PTCDA-Ag interaction is proposed. This conjecture is supported by previous TPD,[16,18] UPS,[18] NEXAFS,[18] STM,[17,51] LEED[16] experiments, and is corroborated by *ab initio* calculations.[20,62]

In the light of present and previous experimental and theoretical results the bonding mechanism of PTCDA/Ag(110) involves two main chemical interaction channels, which interact in a synergistic way.[20] On the one hand, the hybridization of molecular and substrate orbitals, with the associated charge transfer from the substrate to the former LUMO, leads to the bonding of PTCDA with the Ag surface. This interaction channel involves the perylene core where the LUMO is primarily located. Interestingly, DFT calculations also show a weak chemical interaction of perylene C atoms and Ag atoms underneath. On the other hand, the covalent bonding of the functional groups via the oxygen atoms pulls the molecule towards the substrate, such that part of the perylene core experiences Pauli repulsion from the substrate. Hence, the PTCDA molecule bends as NIXSW experiments reveal. To conclude, we have shown that the accurate and detailed structure of PTCDA/Ag(110) from NIXSW provides a broader and deeper insight into the delicate balance of interactions at molecule/metal interfaces.

ACKNOWLEDGMENTS

We thank J. Zegenhagen, B. Detlefs, and Y. Mi (ESRF) for helpful discussions and experimental support. Financial support by the ESRF and the DFG under Projects SFB 624, SFB 813, SO 407/6-1, and TA 244/3-2 is acknowledged.

*g.mercurio@fz-juelich.de

[1] J. Zegenhagen, Surf. Sci. Rep. **18**, 202 (1993).
[2] D. P. Woodruff, Rep. Prog. Phys. **68**, 743 (2005).
[3] F. S. Tautz, Prog. Surf. Sci. **82**, 479 (2007).
[4] S. K. M. Henze, O. Bauer, T.-L. Lee, M. Sokolowski, and F. Tautz, Surf. Sci. **601**, 1566 (2007).
[5] A. Hauschild, K. Karki, B. C. C. Cowie, M. Rohlfing, F. S. Tautz, and M. Sokolowski, Phys. Rev. Lett. **94**, 036106 (2005).
[6] A. Hauschild, R. Temirov, S. Soubatch, O. Bauer, A. Schöll, B. C. C. Cowie, T.-L. Lee, F. S. Tautz, and M. Sokolowski, Phys. Rev. B **81**, 125432 (2010).
[7] L. Kilian, A. Hauschild, R. Temirov, S. Soubatch, A. Schöll, A. Bendounan, F. Reinert, T.-L. Lee, F. S. Tautz, M. Sokolowski, and E. Umbach, Phys. Rev. Lett. **100**, 136103 (2008).
[8] A. Gerlach, S. Sellner, F. Schreiber, N. Koch, and J. Zegenhagen, Phys. Rev. B **75**, 045401 (2007).

[9]M. Sugiyama, S. Maeyama, S. Heun, and M. Oshima, Phys. Rev. B **51**, 14778 (1995).
[10]G. Jackson, J. Lüdecke, D. Woodruff, A. Chan, N. Singh, J. McCombie, R. Jones, B. Cowie, and V. Formoso, Surf. Sci. **441**, 515 (1999).
[11]G. J. Jackson, D. P. Woodruff, R. G. Jones, N. K. Singh, A. S. Y. Chan, B. C. C. Cowie, and V. Formoso, Phys. Rev. Lett. **84**, 119 (2000).
[12]G. Jackson, S. Driver, D. Woodruff, N. Abrams, R. Jones, M. Butterfield, M. Crapper, B. Cowie, and V. Formoso, Surf. Sci. **459**, 231 (2000).
[13]C. Fisher, D. Woodruff, R. Jones, B. Cowie, and V. Formoso, Surf. Sci. **496**, 73 (2002).
[14]K.-U. Weiss, R. Dippel, K.-M. Schindler, P. Gardner, V. Fritzsche, A. M. Bradshaw, A. L. D. Kilcoyne, and D. P. Woodruff, Phys. Rev. Lett. **69**, 3196 (1992).
[15]K.-U. Weiss, R. Dippel, K.-M. Schindler, P. Gardner, V. Fritzsche, A. M. Bradshaw, D. P. Woodruff, M. C. Asensio, and A. R. González-Elipe, Phys. Rev. Lett. **71**, 581 (1993).
[16]C. Seidel, C. Awater, X. D. Liu, R. Ellerbrake, and H. Fuchs, Surf. Sci. **371**, 123 (1997).
[17]K. Glöckler, C. Seidel, A. Soukopp, M. Sokolowski, E. Umbach, M. Böhringer, R. Berndt, and W. D. Schneider, Surf. Sci. **405**, 1 (1998).
[18]Y. Zou, L. Kilian, A. Schöll, T. Schmidt, R. Fink, and E. Umbach, Surf. Sci. **600**, 1240 (2006).
[19]O. Bauer, G. Mercurio, M. Willenbockel, N. Fairley, W. Reckien, C. H. Schmitz, B. Fiedler, S. Soubatch, T. Bredow, F. S. Tautz, and M. Sokolowski (unpublished).
[20]O. Bauer, G. Mercurio, M. Willenbockel, W. Reckien, C. H. Schmitz, B. Fiedler, S. Soubatch, T. Bredow, F. S. Tautz, and M. Sokolowski, Phys. Rev. B **86**, 235431 (2012).
[21]1 ML is defined as the sample coverage corresponding to a brick-wall PTCDA layer covering the entire metal surface.
[22]C. Seidel, J. Poppensieker, and H. Fuchs, Surf. Sci. **408**, 223 (1998).
[23]D. Braun, A. Schirmeisen, and H. Fuchs, Surf. Sci. **575**, 3 (2005).
[24]E. Umbach, K. Glöckler, and M. Sokolowski, Surf. Sci. **402–404**, 20 (1998).
[25]M. Cardona and L. Ley, in *Photoemission in Solids I*, edited by M. Cardona and L. Ley, Topics in Applied Physics, Vol. 26 (Springer-Verlag, Berlin, 1978), pp. 80–81.
[26]B. E. Warren, in *X-ray Diffraction* (Dover, Mineola, NY, 1990), pp. 27–35.
[27]M. B. Trzhaskovskaya, V. I. Nefedov, and V. G. Yarzhemsky, At. Data Nucl. Data Tables **77**, 97 (2001).
[28]A. Schöll, Y. Zou, M. Jung, T. Schmidt, R. Fink, and E. Umbach, J. Chem. Phys. **121**, 10260 (2004).
[29]N. Fairley, CASAXPS, version 2.3.16, Casa Software Ltd, Bay House, 5 Grosvenor Terrace, Teignmouth, Devon TQ14 8NE, United Kingdom.
[30]G. Mercurio, E. R. McNellis, R. J. Maurer, S. Hagen, F. Leyssner, J. Meyer, M. Wolf, P. Tegeder, S. Soubatch, K. Reuter, and F. S. Tautz (unpublished).
[31]TORRICELLI is an XSW data analysis and simulation program written by G. Mercurio; copies can be obtained from s.tautz@fz-juelich.de.
[32]G. Mercurio, Study of Molecule-Metal Interfaces by Means of the Normal Incidence X-ray Standing Wave Technique, Schriften des Forschungszentrums Jülich, Reihe Schlüsseltechnologien, Vol. 49 (Dissertation, RWTH Aachen University, 2012), available at http://www.fz-juelich.de/zb/juwel
[33]G. Mercurio, N. Fairley, S. Soubatch, and F. S. Tautz (unpublished).
[34]O. Bauer, and M. Sokolowski, XSWAVES—An XSW Data Evaluation Routine for ORIGIN 8, version 2.31 (2010), available from: http://www.thch.unibonn.de/pctc/sokolowski/XSWAVES/XSWAVES_index.html
[35]K. Harrison and L. B. Hazell, Surf. Interface Anal. **18**, 368 (1992).
[36]G. K. Wertheim, M. A. Butler, K. W. West, and D. N. E. Buchanan, Rev. Sci. Instrum. **45**, 1369 (1974).
[37]J. J. Lee, C. J. Fisher, D. P. Woodruff, M. G. Roper, R. G. Jones, and B. C. C. Cowie, Surf. Sci. **494**, 166 (2001).
[38]A. Gerlach, F. Schreiber, S. Sellner, H. Dosch, I. A. Vartanyants, B. C. C. Cowie, T.-L. Lee, and J. Zegenhagen, Phys. Rev. B **71**, 205425 (2005).
[39]I. A. Vartanyants and J. Zegenhagen, Solid State Commun. **113**, 299 (1999).
[40]A. Jablonski, F. Salvat, and C. J. Powell, *NIST Electron Elastic-Scattering Cross-Section Database*, Tech. Rep., Version 3.1 (National Institute of Standards and Technology, Gaithersburg, MD, 2003).
[41]I. Vartanyants, T.-L. Lee, S. Thiess, and J. Zegenhagen, Nucl. Instrum. Methods Phys. Res.. Sect. A **547**, 196 (2005).
[42]C. Stadler, S. Hansen, F. Pollinger, C. Kumpf, E. Umbach, T.-L. Lee, and J. Zegenhagen, Phys. Rev. B **74**, 035404 (2006).
[43]In Ref. 20 nondipolar parameters for Ag3*d* are calculted assuming $\Delta = 0$. Therefore, slightly different P_c and F_c for Ag3*d* result.
[44]P. J. Cumpson and M. P. Seah, Surf. Interface Anal. **18**, 345 (1992).
[45]W. H. Press, S. A. Teukolsky, W. T. Vetterling, and B. P. Flannery, *Numerical Recipes: The Art of Scientific Computing*, 3rd ed. (Cambridge University Press, Cambridge, 2007).
[46]J. R. Taylor, *An Introduction to Error Analysis: The Study of Uncertainties in Physical Measurements* (University Science Books, South Orange, NJ, 1997).
[47]S. L. Meyer, *Data Analysis for Scientists and Engineers* (Wiley, New York, 1975).
[48]W. Grenier, *Classical Mechanics*, 2nd ed. (Springer, Berlin, 2009).
[49]D. A. Shirley, in *Photoemission in Solids I*, edited by M. Cardona and L. Ley, Topics in Applied Physics, Vol. 26 (Springer-Verlag, Berlin, 1978), p. 193.
[50]V. B. Nascimento, E. A. Soares, V. E. de Carvalho, E. L. Lopes, R. Paniago, and C. M. C. de Castilho, Phys. Rev. B **68**, 245408 (2003).
[51]M. Böhringer, W. D. Schneider, K. Glöckler, E. Umbach, and R. Berndt, Surf. Sci. **419**, L95 (1998).
[52]M. J. Frisch *et al.*, GAUSSIAN 03, Revision C.02 (Gaussian, Inc., Wallingford, CT, 2004).
[53]B3LYP functional, LANL2DZ basis set was used.
[54]B. Cordero, V. Gomez, A. E. Platero-Prats, M. Reves, J. Echeverria, E. Cremades, F. Barragan, and S. Alvarez, Dalton Trans. **21**, 2832 (2008).
[55]A. Bondi, J. Phys. Chem. **68**, 441 (1964).
[56]F. Schreiber, A. Gerlach, N. Koch, E. Zojer, M. Sokolowski, F. S. Tautz, M. Rohlfing, and E. Umbach, Phys. Rev. Lett. **99**, 059601 (2007).
[57]I. Kröger, B. Stadtmüller, C. Stadler, J. Ziroff, M. Kochler, A. Stahl, F. Pollinger, T.-L. Lee, J. Zegenhagen, F. Reinert, and C. Kumpf, New J. Phys. **12**, 083038 (2010).

[58]J. Ikonomov, O. Bauer, and M. Sokolowski, Surf. Sci. **602**, 2061 (2008).
[59]J. Ikonomov, P. Bach, R. Merkel, and M. Sokolowski, Phys. Rev. B **81**, 161412 (2010).
[60]M. Böhringer, W.-D. Schneider, R. Berndt, K. Glöckler, M. Sokolowski, and E. Umbach, Phys. Rev. B **57**, 4081 (1998).
[61]J. Ikonomov, C. H. Schmitz, and M. Sokolowski, Phys. Rev. B **81**, 195428 (2010).
[62]A. Abbasi and R. Scholz, J. Phys. Chem. C **113**, 19897 (2009).
[63]J. P. Perdew, K. Burke, and M. Ernzerhof, Phys. Rev. Lett. **77**, 3865 (1996).
[64]S. Grimme, S. Ehrlich, and L. Goerigk, J. Comput. Chem. **32**, 1456 (2011).
[65]W. Reckien, F. Janetzko, M. F. Peintinger, and T. Bredow, J. Comput. Chem. **33**, 2023 (2012).
[66]M. Rohlfing, R. Temirov, and F. S. Tautz, Phys. Rev. B **76**, 115421 (2007).
[67]F. S. Tautz, S. Sloboshanin, J. A. Schaefer, R. Scholz, V. Shklover, M. Sokolowski, and E. Umbach, Phys. Rev. B **61**, 16933 (2000).
[68]F. S. Tautz, S. Sloboshanin, V. Shklover, R. Scholz, M. Sokolowski, J. A. Schaefer, and E. Umbach, Appl. Surf. Sci. **166**, 363 (2000).